Coastal Engineering 57 (2010) 779–794

Contents lists available at ScienceDirect

Coastal Engineering

journal homepage: www.elsevier.com/locate/coastaleng

Numerical simulation of waves generated by landslides using a multiple-fluid Navier–Stokes model

Stéphane Abadie [a,*], Denis Morichon [a], Stéphan Grilli [b], Stéphane Glockner [c]

[a] Université de Pau et des Pays de l'Adour, Laboratoire de Sciences Appliquées au Génie Civil et au Génie Côtier JE2519, Allée du parc Montaury, 64600 Anglet, France
[b] Department of Ocean Engineering, University of Rhode Island, Narragansett, RI 02882, USA
[c] Université de Bordeaux I, UMR 8508 TREFLE — ENSCBP — 16, avenue Pey-Berland, 33607 PESSAC Cedex, France

ARTICLE INFO

Article history:
Received 15 February 2008
Received in revised form 3 March 2010
Accepted 16 March 2010

Keywords:
Tsunami
Waves
Landslide
Navier–Stokes
Volume of Fluid
Numerical model

ABSTRACT

This work reports on the application and experimental validation, for idealized geometries, of a multiple-fluid Navier–Stokes model of waves generated by rigid and deforming slides, with the purpose of improving predictive simulations of landslide tsunamis. In such simulations, the computational domain is divided into water, air, and slide regions, all treated as Newtonian fluids. For rigid slides, a penalty method allows for parts of the fluid domain to behave as a solid. With the latter method, the coupling between a rigid slide and water is implicitly computed (rather than specifying a known slide kinematics). Two different Volume of Fluid algorithms are tested for tracking interfaces between actual fluid regions. The simulated kinematics of a semi-elliptical block, moving down a water covered plane slope, is first compared to an earlier analytical solution. Results for the vertical fall of a rectangular block in water are then compared to earlier experimental results. Finally, more realistic simulations of two- and three-dimensional wedges sliding down an incline are compared to earlier experiments. Overall, in all cases, solid block velocities and free surface deformations are accurately reproduced in the model, provided that a sufficiently resolved discretization is used. The potential of the model is then illustrated on more complex scenarios involving waves caused by multi-block or deformable slides.

1. Introduction

Landslide generated impulse waves, also referred to as *landslide tsunamis* (Ward, 2001) are water waves created by mass flows, either initiated underwater or subaerial. Such waves may occur both in the ocean and in more restricted water bodies, such as lakes, reservoirs, or fjords. Submarine landslides (e.g., Grilli and Watts, 1999, 2005; Watts et al., 2003; Lovholt et al., 2005), or slumps (e.g., Heinrich et al., 2001; Tappin et al., 2008), rock/debris flows (e.g., Fritz et al., 2001), volcano flank collapses (e.g., Ward and Day, 2001; Pararas-Carayannis, 2002; Gisler et al., 2006; Løvholt et al., 2008; Abadie et al., 2009), and pyroclastic flows (e.g., Tinti et al., 2006) are among the main geophysical mechanisms responsible for landslide tsunami generation. In view of typical slide volumes, tsunami hazard in terms of coastal run-up is usually limited to the near-field generation area. However, recent studies (e.g., Masson et al. 2002, 2006; Pareschi et al., 2006) indicate that volcano collapses involving huge volumes (in the hundreds of km^3 of material) have occurred in the past, which could have the potential of triggering tsunamis large enough to strike coasts far away from the generation area, even over transoceanic distances (e.g., Ward and Day, 2001; Løvholt et al., 2008).

Recent experimental works (e.g., Fritz, 2002; Grilli and Watts, 2005; Liu et al., 2005; Enet and Grilli, 2005, 2007) show that complex wave fields can be generated by underwater or subaerial slides. The correct description of these waves near the source is the key to the accurate modeling and prediction of tsunami propagation, resulting coastal hazard, and eventual mitigation. Due to the many spatial and temporal scales involved, in operational tsunami forecast, one typically uses different types of models to estimate waves generated near the source, due to one of the potential tsunami generation mechanisms discussed above, to propagate these over oceanic distance both on- and offshore (usually using a two-dimensional (2D) horizontal long wave model), and to predict coastal impact. It is the purpose of this work to contribute to the improvement of tsunami source modeling, in the context of tsunami generation by underwater and subaerial slides.

Landslide tsunami generation includes processes of slide initiation (or triggering), motion, interaction with water and air, and induced water surface deformation; the latter sometimes involving breaking and air entrapment. Landslide triggering, which will be assumed beyond the scope of this work, is governed by seismology, geology and marine geomechanics. (In this respect, see for instance the recent stochastic work of Grilli et al., 2009.) Slide motion depends strongly

* Corresponding author. Tel.: +33 5 59 57 44 21; fax: +33 5 59 57 44 39.
E-mail addresses: stephane.abadie@univ-pau.fr (S. Abadie), denis.morichon@univ-pau.fr (D. Morichon), grilli@oce.uri.edu (S. Grilli), glockner@enscbp.fr (S. Glockner).

0378-3839/$ – see front matter © 2010 Elsevier B.V. All rights reserved.
doi:10.1016/j.coastaleng.2010.03.003

on the material properties as well as on site geometry (e.g., Varnes, 1978; Walder et al., 2003; Grilli and Watts, 2005; Watts et al., 2005). Interactions between slide and water start upon slide initiation for underwater events, or when the slide penetrates water for subaerial cases. Considering the Reynolds numbers involved in such geophysical phenomena, the water flow will be turbulent throughout slide motion. The air or water flow surrounding the slide has a significant effect on slide motion, through hydrodynamic drag forces. Such feedback forces are most significant for subaerial slides, particularly for violent cases, since air may be entrapped during the penetration phase (Fritz et al., 2001). Air flow is also susceptible to be of importance for wave dissipation if breaking occurs (Hoque, 2002).

Many studies have been devoted to studying landslide generated impulse waves. Analytical solutions have been obtained in some simple idealized cases (e.g., Noda, 1970; Hunt, 1988; Liu et al., 2003; Ward, 2001; Haugen et al., 2005). Experimental works have mostly tried to relate non-dimensional numbers associated with landslide motion to wave characteristics and associated run-up (Watts, 1997; Fritz, 2002; Walder et al., 2003; Fritz et al., 2004; Grilli and Watts, 2005; Watts et al., 2005; Liu et al., 2005; Enet and Grilli, 2005, 2007). Most of these studies are 2D, with a few based on three-dimensional (3D) experiments (e.g., Liu et al., 2005; Enet and Grilli, 2005, 2007). Numerical studies of landslide tsunamis have been based on a variety of models and hypotheses regarding slide geometry and behavior. Such studies also differ with respect to slide motion, which is either specified or directly simulated as part of the model solution. Thus, in simulations by Harbitz (1992), Pelinovsky and Poplavsky (1996), Grilli and Watts (1999, 2005), Watts et al. (2005), and Enet and Grili (2005), Lynett and Liu (2005) and Liu et al. (2005), to name a few, the center of mass motion of a rigid slide was specified based on a dynamic force balance based on Newton's first law, involving, weight, buoyancy, friction, hydrodynamic drag and inertia forces, with a few empirical coefficients based on theories or experiments. This approach was well validated experimentally for rigid slides of idealized shape (Enet et al., 2003; Enet and Grilli, 2005, 2007; Grilli and Watts 2005; Watts et al., 2005). Notably, this approach was used as part of (full dynamics) fully nonlinear 2D and 3D potential flow simulations of underwater landslide tsunamis (Grilli and Watts, 1999, 2005; Grilli et al., 2002, 2010; Enet and Grilli, 2005), whose results were used to develop semi-empirical landslide tsunami sources and perform successful tsunami case studies (e.g., Watts et al., 2003, 2005; Tappin et al., 2008). While useful and accurate to study rigid underwater slides or slumps of simple shapes, and specify approximate *ad hoc* sources in tsunami propagation models, such an approach however has severe limitations: (1) it cannot be used in the case of subaerial landslides, as water–slide interactions are more complex than the physics included in both Newton's law and inviscid flow theory; (2) the study of actual scenarios requires experiments to determine the corresponding empirical added mass and drag coefficients or to use typical values for entire classes of slides. (This is discussed in detail in Watts et al., 2005.)

Formulations also differ based on equations used to model fluid motion. Jiang and Leblond (1992, 1993) used nonlinear shallow water equations to describe slide and water motion. This approach was applied by other authors (Imamura and Imteaz, 1995; Heinrich et al., 2001) to describe underwater landslide tsunami. But shallow water equations have intrinsic limitations such as no vertical accelerations, which in theory prevents them from being applied to most subaerial cases where strong vertical accelerations do occur. As for potential flow models, which solve Navier–Stokes (NS) equations for irrotational flows, although these have been showed to be highly accurate for simulating tsunamis generated by smooth and rigid underwater slides (e.g., Grilli et al., 2002, 2010; Grilli and Watts, 2005), they cannot be applied to cases where strong vorticity is created by flow separation or interface reconnection, which both occur in subaerial slide cases. In such cases, more sophisticated flow dynamics models must be used and several attempts were made in this direction. Among the works in which slide velocity was *a priori* prescribed, Heinrich (1992) used NS equations with a Volume of Fluid (VOF) method to describe tsunamis generated by rigid blocks. The slide velocity measured experimentally was used as an input in the numerical model. A good agreement was found between experiments and simulations. Yuk et al. (2006) presented a numerical study based on the Reynolds Averaged NS (RANS) equations. Numerical simulations were compared to experimental results obtained by Heinrich (1992). The slide motion was also prescribed in this case and reasonably good agreement was achieved. Liu et al. (2005) presented Large Eddy Simulations (LES) of three-dimensional sliding masses using the Smagorinsky's subgrid model. Slide motion was specified in the model from experimental results. Numerical results matched experimental results quite well in this first 3D simulation of subaerial rigid slides.

Few numerical models have been proposed to date, which can describe the full coupling between slide and water, together with the surrounding viscous/turbulent water flow. Among these, Assier Rzadkiewicz et al. (1997) proposed a 2D model, which considered a mixture of water and sediment. The free surface motion was represented by a VOF algorithm and the sediment was considered as a Bingham fluid. Rigid slide motion was implicitly obtained by setting a very high value of the yield strength in the rheological model. The experiments of Heinrich (1992) were simulated and free surface as well as slide motion matched experimental values quite well. Monaghan and Kos (2000) and Panizzo and Dalrymple (2004) used a Smoothed Particle Hydrodynamics (SPH) method to simulate landslide generated waves. In Monaghan and Kos (2000), the waves were generated by the vertical drop of a rigid square block. Simulations were compared to experiments (also reported later in this paper) and shown to be able to reproduce block motion, wave height, and also features of the complex free surface flow close to the solid. Note that a comparison of VOF and SPH method for this case was reported by Yim et al. (2008).

Air motion has rarely been considered in subaerial landslide models. Among the authors who have included this effect, Mader and Gittings (2002, 2003) and Gisler et al. (2006) solved compressible multi-material NS equations, with a Continuous Adaptive Mesh Refinement, and Quecedo et al. (2004) solved NS equations with indicator functions, using the Finite Element Method. The latter authors applied their model to the Lituya Bay case study and qualitatively compared their results to available experimental measurements.

Here, we present a new advanced model, referred to as *Thetis*, based on Direct Numerical Simulation (DNS) of NS equations. Water, air, and slide are treated as fluids, whose interfaces are tracked using the VOF method. A penalty approach is used to implicitly compute slide motion. By contrast with earlier published work, we concentrate here on validating the implicit computation of slide–water interactions, which yields slide motion, for the more idealized case of non-deformable slides. Although actual slides, especially subaerial ones, are deformable, rigid slides have more often been used in laboratory experiments, in an attempt to simplify the problem and provide reference data for numerical models (e.g., Liu et al., 2005; Enet et al., 2003; Enet and Grilli, 2005, 2007). Here, similarly, we use such data to validate the newly proposed model. Once this is done, the model, which is general, can be applied to deformable slides. Validation of this latter aspect, however, is still in progress and only a few illustrative results with deformable slides are shown at the end of the paper. Finally note, earlier potential flow simulations for rigid and deforming underwater slides, indicate that key features of tsunami generation are mostly governed by the early slide kinematics, and particularly the initial slide acceleration, which is not significantly affected by large deformations that may occur later during slide motion (Grilli and Watts, 2005; Watts et al., 2005). Hence, studying rigid slides has intrinsic merit for such more general underwater slide cases.

The paper is organized as follows: in Section 2, we present the model equations and numerical methods, in Section 3, we present validation cases, and finally Section 4 is devoted to a discussion.

2. The model

In the present applications, we perform direct numerical simulations (DNS) of flows composed of three separated phases: water, air and slide. This approach, which does not use a subscale turbulence model, is justified since, during a rapid generation process, subaerial (not too elongated) landslide impulse waves are to a large extent generated by pressure forces and turbulence effects are expected to be of second-order as compared to other processes. Thus, even though all the scales of turbulence are not well resolved in the computations, the simulated waves are nevertheless expected to be realistic enough to allow for an accurate prediction of landslide tsunami sources.

The representation of turbulence by LES, using the Mixed Scale Model of Sagaut (1996) and Lubin et al. (2006), was also tested, but found to yield slightly less accurate result. In fact, we found that the LES method was adding spurious dissipation to the already significant (and thus sufficient) numerical dissipation inherent to the model algorithm.

For simplicity, in the present applications, all phases are considered to be Newtonian fluids, although standard non-Newtonian behavior is also implemented in the model. Following Kataoka (1986), we consider multiphase flows using a single fluid formulation governed by NS equations, in which density and viscosity are calculated as a function of location:

$$\nabla\cdot\boldsymbol{u} = 0 \tag{1}$$

$$\rho\left(\frac{\partial \boldsymbol{u}}{\partial t} + (\boldsymbol{u}\cdot\nabla)\boldsymbol{u}\right) = -\nabla p + \rho\boldsymbol{g} + \nabla\cdot\left(\mu\left(\nabla\boldsymbol{u} + \nabla\boldsymbol{u}^t\right)\right) \tag{2}$$

in which u_i and p are the velocity and pressure.

The above governing equations are completed by two advection equations specifying that each interface in the model moves with the fluid velocity:

$$\frac{\partial C_w}{\partial t} + (\boldsymbol{u}\cdot\nabla)C_w = 0 \tag{3}$$

$$\frac{\partial C_s}{\partial t} + (\boldsymbol{u}\cdot\nabla)C_s = 0 \tag{4}$$

where C_w is the local volume fraction of water (i.e., 1 if water is present and 0 otherwise) and C_s the local volume fraction of the slide material (similarly defined). Air is assumed to fill every cell in which C_w and C_s are 0.

The local fluid density and viscosity (w for water, s for slide and a for air) are defined as a function of the volume fractions by:

$$\begin{array}{l}\rho = \rho_w \quad \mu = \mu_w \quad \text{if } C_w > 0.5\\ \rho = \rho_s \quad \mu = \mu_s \quad \text{if } C_s > 0.5\\ \rho = \rho_a \quad \mu = \mu_a \quad \text{else}\end{array} \tag{5}$$

(Note that, although the method is detailed here for three fluids, this does not represent a limitation and one could easily apply it to k fluids, by solving $(k-1)$ advection equations.)

In the model, we use two methods of fluid–fluid interface representation and time updating:

1. The first method is the Piecewise Linear Interface Calculation (PLIC) algorithm (Young et al., 1982; Li, 1995; Abadie et al., 1998; Liu, 1999; Breil and Caltagirone, 2000), which is based on a mixed Eulerian–Lagrangian formulation. In the PLIC algorithm, we first define a piecewise linear approximation of the fluid interfaces, using values of C_w and C_s integrated over the neighboring mesh cells. Then, the position of the linear segments representing fluid interfaces is updated by advecting these based on an interpolation of the local fluid velocity. Finally, updated values of the water and slide volume fractions are calculated, based on the new interface locations within each cell. This algorithm is non-diffusive, which implies that interfaces remain discontinuous all along the computations. This method is hereafter referred to as NS-PLIC.
2. The second method is the Total Variation Diminishing (TVD) superbee scheme (LeVeque, 1990; Vincent and Caltagirone, 1999). In this case, Eqs. (3) and (4) are directly solved using a Lax Wendroff Scheme, modified by using the TVD theory. The resulting scheme is second-order where the volume fraction is regular and first-order close to discontinuities, which allows to preserve sharp discontinuities through time updating, without triggering oscillations such as observed with higher-order schemes. This method is hereafter referred to as NS-TVD.

With both methods, updated local values of density and viscosity are calculated for each cell containing an interface, using Eq. (5), in which C_w and C_s are replaced by the corresponding cell volume fractions. Both methods' performance will be compared in the applications for three test cases.

To solve the velocity/pressure coupling in the equations, we use the augmented Lagrangian method (Fortin and Glowinski, 1982), a constrained minimization method that was successfully applied to turbulent multiphase flows (Lubin et al., 2006; Vincent et al., 2007a,b). Fortin and Glowinski (1982) give numerous applications of this method to the solution of partial differential equations, particularly Stokes and NS equations, formulated as a velocity–pressure problem requiring the computation of a saddle point $(\mathbf{u},p)$, associated with the augmented Lagrangian of the problem (i.e., a minimization–maximization). Specifically, in the equations, pressure is treated as a Lagrangian multiplier and the fluid incompressibility constraint is implicitly specified into the momentum equations. The $(\mathbf{u},p)$ saddle point is iteratively computed using an Uzawa algorithm, until, for the k-th iteration $(\mathbf{u}^k,p^k)$, the divergence of the velocity field, div $\mathbf{u}<\varepsilon$, with ε small:

Initialization

$$u^{k=0} = u^n, p^{k=0} = p^n$$

Iterations

for $k=0, K-1$

computation of $\boldsymbol{u}^{k+1}$ solution of

$$\begin{aligned}\rho^n\left(\frac{\boldsymbol{u}^{k+1}}{\Delta t} + \boldsymbol{u}^k\cdot\nabla\boldsymbol{u}^{k+1}\right) = {} & \rho^n g - \nabla p^k \\ & + \nabla\cdot\left[(\mu)\left(\nabla\boldsymbol{u}^{k+1} + \nabla^t\boldsymbol{u}^{k+1}\right)\right] \\ & + \rho^n\left(\frac{\boldsymbol{u}^n}{\Delta t}\right) + \alpha\nabla\left(\nabla\cdot\boldsymbol{u}^{k+1}\right)\end{aligned} \tag{6}$$

updating of p^{k+1} with:

$$p^{k+1} = p^k - \beta\cdot u^{k+1}$$

Solution

$$u^{n+1} = u^K, p^{n+1} = p^K.$$

The choice of parameters α and β in the algorithm is crucial for achieving convergence in incompressibility. In practice, for single fluid

problems, the use of a constant value of α, on the order of ρ provides an accurate solution of both momentum and incompressibility equations. Whenever several fluids with large density gradients are simulated, however, α may have to vary in time and space; otherwise the flow in one of the fluids is in certain cases not properly solved for (Lubin et al., 2006). Here, we automatically compute α ($\mathbf{x}$,t) as detailed in Vincent et al. (2007b), based on an analysis of the algebraic linear system resulting from the discretization of the equations of motion. Accordingly, at each time step, the best local value of α is determined in order to always be 2 or 3 orders of magnitude larger than the other terms in Eq. (6); then β is set equal to α. We found that 1 to 4 iterations must be performed at each time step to achieve low velocity divergence levels.

The rigidity of solid zones is achieved by specifying a sufficiently large value of the viscosity (values of 10^4 to 10^{10} Pa s were typically used). This so-called viscous penalty approach, which belongs to fictitious domains methods (Peskin, 1977), has been validated in the model for the computation of the free fall of a solid sphere at moderate to high Reynolds numbers (Vincent et al., 2007b; Randrianarivelo et al., 2005). This method is applied in the present paper and validated for a more complex three-phase flow.

The above equations are discretized on a staggered structured grid, using the finite volume approach. Advection terms are expressed in a hybrid Upwind-Centered scheme and viscous terms are defined using a second-order centered scheme. Higher-order methods such as the *centered* and the *QUICK* schemes were found to be unstable or to induce oscillations in the velocity field, respectively.

The resulting linear algebraic system of equations obtained for each time step is solved using the MUltifrontal Massively Parallel Sparse direct solver (MUMPS) by Amestoy et al. (2000). This solver is five times faster than our implementation of the BiCGstab iterative solver associated to an ILU preconditioner (Van der Vorst, 1992) and ensures an accuracy close to that of the computer.

3. Validation cases

3.1. Landslide motion in air and water

The motion of a subaerial landslide is typically divided into three phases: (i) after triggering, the slide propagates over some distance, only interacting with air; (ii) the slide penetrates water, while a part of it still interacts with air; and (iii) the whole slide becomes submerged in water and its effect on the free surface decreases with time.

In this section, we aim at separately validating the model for the first and third phases of motion of a subaerial rigid slide. The second phase will be addressed in the next section (Section 3.2). For those two phases, the slide is only surrounded by one fluid, either air or water, and the free surface influence on its motion is small and hence can be neglected in this validation. Note that basal friction, which may play an important role in this phenomenon in natural conditions, is neglected here to focus on slide/water interaction phenomena. The effect of basal friction could easily be introduced in the model by simply reducing gravity in the rigid slide by an amount corresponding to global frictional effects. Fig. 1 shows the fluid domain considered in these computations, which consists of a rectangle of length $L_d = 7$ m and height $H_d = 0.75$ m. The slide shape is semi-elliptical, with length $L = 1$ m, and thickness $T = 0.25$, similar to the model slide used in the earlier submarine/subaerial landslides experiments of Grilli and Watts (1999, 2005), which will be used as a reference to estimate hydrodynamic parameters such as drag or added mass coefficient. As shown in Fig. 1, to simulate a slide moving down a plane slope in the model, the gravity vector is set at an angle α with respect to the z direction.

The rigid slide law of motion is governed by the following equation expressing the balance between slide acceleration, fluid added mass, gravity, buoyancy and drag (e.g., Grilli and Watts, 2005):

$$(m + m_{\text{add}})\ddot{x} = (m - \rho V_s) g \sin(\alpha) - \frac{1}{2}\rho C_D T \dot{x}^2. \tag{7}$$

In Eq. (7), m is the slide mass, m_{add} the inertia effects of the surrounding fluid on slide motion, expressed as a fluid added mass, which for a semi-elliptical shape in an infinite fluid is equal to $1/2\rho\pi T^2$, with ρ denoting the fluid density, V_s the slide volume and C_D the sum of the pressure and friction drag coefficients ($C_D \sim 0.2$ after White, 2002).

Slide density ρ_s is here arbitrarily set to 2000 kg/m^3. When the slide moves in the air, added mass, buoyancy and drag forces are assumed to be negligible with respect to gravity, and Eq. (7) becomes:

$$m\ddot{x} = mg \sin(\alpha) \tag{8}$$

which yields a simply accelerated slide motion down the slope:

$$x(t) = \frac{1}{2} g \sin(\alpha) t^2. \tag{9}$$

3.1.1. Slide motion in air

We simulated the aerial phase (i) of a semi-elliptical 2D slide moving down an incline using the NS-TVD model, for four slope angles $\alpha = 15°, 30°, 45°$ and $60°$. The computational grid had 700×75 cells, yielding non-dimensional grid sizes of $\Delta x/L = \Delta z/L = 0.01$. Free slip boundary conditions were specified on every boundary, except along the upper boundary over which an open boundary condition was applied to the velocity. Initially, the slide center of mass was located at $X_0 = 1$ m, and simulations were stopped when it reaches $X_g = 4$ m, so that the velocity field is not affected by the right side boundary condition.

Slide viscosity was set to 10^{10} Pa s, yielding a quasi-rigid behavior. The volume tracking was performed using the TVD superbee scheme. Twenty iterations with a very small constant time step of 0.01 s were first performed to ensure a proper initiation of slide motion, then time steps were computed so that the maximum mesh Courant number be less than 1.

Fig. 2 compares model results to Eq. (9) for the four simulated cases. The agreement is quite good, and RMS differences ($\sqrt{\sum_{i=1}^{n} (x_{th_i} - x_{si_i})^2 / n}$) between theoretical and simulated center of mass motions are found to monotonically increase from 8.10^{-3} to 11.10^{-3} m with increasing slope values. After moving three times its length, theoretical and simulated locations of the slide center of mass only differ by about one grid size (i.e.

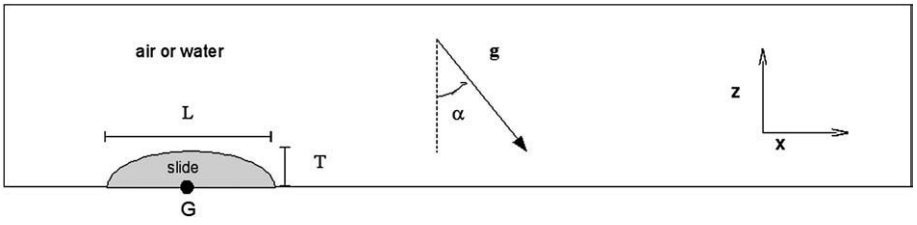

Fig. 1. Sketch of the slide case simulated.

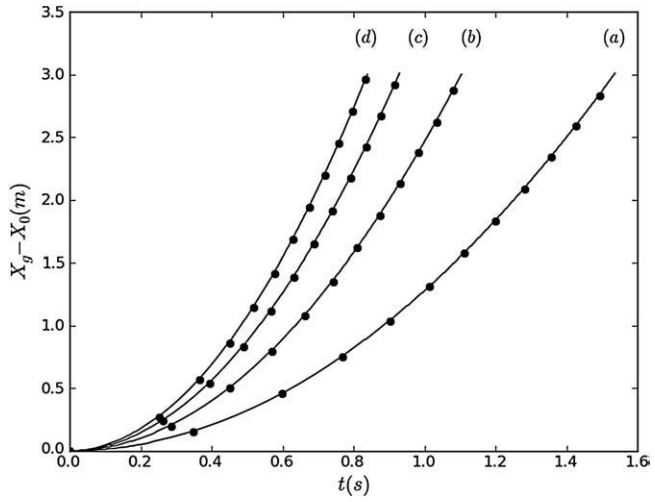

Fig. 2. 2D NS-TVD simulations for a semi-elliptical rigid body surrounded by air sliding down an incline. Time evolution of the center of mass abscissa. (•): analytical Eq. (9), (−): NS-TVD results for α=: (a) 15°, (b) 30°, (c) 45°, and (d) 60°.

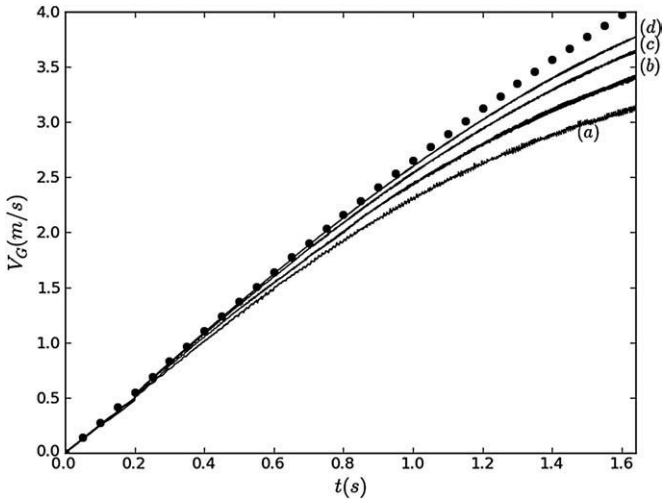

Fig. 4. Semi-elliptical rigid body sliding down an incline underwater ($\alpha = 45°$). Time evolution of slide velocity. (•): obtained by solving Eq. (7) for theoretical values of added mass and drag forces. (−) simulated with the NS-TVD for decreasing cell sizes. (a) $\Delta x^*/L = 0.02$, (b) $\Delta x/L = 0.01$, (c) $\Delta x/L = 0.005$, and (d) $\Delta x/L = 0.003$.

0.01 m). This indicates that the slide aerial stage is properly simulated in the model. Fig. 3 displays the flow streamlines at $t = 1$ s within the slide as well as in the surrounding air for the case $\alpha = 30°$. Within the slide, one can see that the flow is uniform and streamlines are rectilinear, confirming that the slide behaves as a rigid body. At the end of the simulations, the slide length variation is less than 10^{-8} m and the mean relative velocity difference within the slide is about 10^{-9} during simulations.

3.1.2. Slide motion in water

We now simulate the underwater phase (iii) of slide motion, where the force balance is described by the complete Eq. (7), in which each force now plays an important role. Assuming the theoretical values indicated above for the added mass and drag coefficient, slide motion can be calculated as a function of time by integrating Eq. (7), which is done using a fourth-order Runge–Kutta scheme, with a time step of 0.001 s. Fig. 4 compares the theoretical time evolution of slide velocity to NS-TVD model results obtained this way. Numerical parameters are identical to those used in the aerial phase, except that it was found, the Courant number must be less than 0.2 to ensure numerical stability and no deformation of the slide shape. Such spurious deformations would strongly affect hydrodynamic drag and hence slide motion.

To illustrate model convergence towards the theoretical solution, four decreasing mesh sizes were successively used in simulations with $\Delta x^* = \Delta x/L = \Delta z^* = \Delta z/L = 0.02$, 0.01, 0.005 and 0.003, and the slope angle was set to $\alpha = 45°$. Note, the slide center of mass velocity is obtained at each time step by taking the average of "fluid" velocities computed within the slide. As before, simulations were stopped when the slide traveled three times its length.

In Fig. 4 we see that NS-TVD model results clearly converge towards the theoretical solution, when the computational grid is increasingly refined (and time step adjusted accordingly based on the mentioned Courant condition). Relative errors with respect to the theoretical solution, calculated at $t = 0.8$ s, are 11.1%, 7.5%, 3.7% and 1.3% for $\Delta x^* = 0.02$, 0.01, 0.005 and 0.003, respectively. At $t = 1.5$ s, errors have increased to reach 20.4%, 14.1%, 8.7% and 5.6%. Thus, as could be expected, we find that mesh size plays a key role in ensuring accurate numerical results for the underwater slide motion. The fairly slow convergence rate is likely related to the accurate computation of drag forces in the model, which is known to be difficult to achieve in NS models. Usually, accurate drag force computations require using extremely fine meshes, closely matching the body boundary geometry (Gumusel et al., 2006). In the present case, the flow is created by slide motion in a simple Cartesian grid, which hence requires very fine cells. Fig. 5 shows water velocity vectors calculated around the semi-elliptical slide in the slide moving frame of reference in the finer mesh case. (Note, only about 3% of the grid nodes are represented in Fig. 5 for clarity sake.) We see, a fraction of the water volume surrounding the slide is moving at the slide speed (white area). This water volume is related to the added water mass modeled in Eq. (7). The shear flow, responsible for viscous drag is clearly visible just outside the slide boundary. Behind the slide, we observe a short wake with a flow recirculation due to flow separation.

Finally, slightly more accurate results were obtained in this test case when using the NS-PLIC method in the same discretization (Fig. 6). This is likely because the PLIC algorithm of interface reconstruction allows for a finer description of the interface geometry, which cannot be achieved by a direct method such as TVD superbee. Errors on slide velocity calculated at $t = 0.8$ s using the NS-PLIC method were 10.6%, 4.9%, 1.6% and 0.2%, for $\Delta x^* = 0.02$, 0.01, 0.005 and 0.003, respectively. At $t = 1.5$ s, after a distance traveled of about three slide lengths, errors on slide velocity reached 16.8%, 10.6%, 6% and 3.6%, respectively.

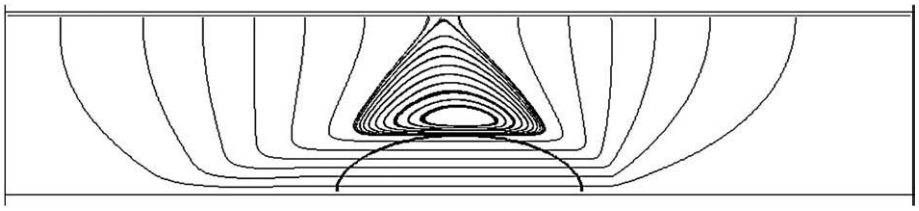

Fig. 3. Slide contour and flow streamlines obtained with the NS-TVD model for the case of Fig. 2 with $\alpha = 30°$ at $t = 1$ s.

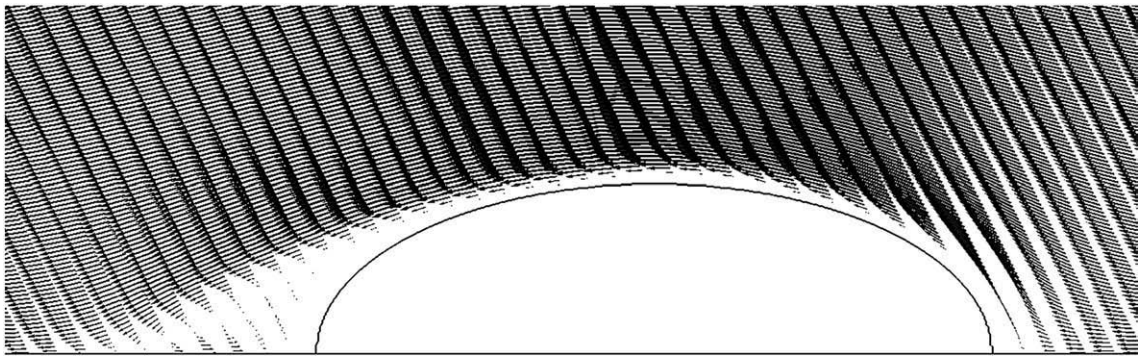

Fig. 5. Semi-elliptical rigid body sliding down an underwater incline ($\alpha = 45°$). Slide motion is left to right. Snapshot of water velocity vectors in the moving frame at $t = 0.5$ s in the finer mesh case using the NS-TVD model.

3.2. Strong slide interaction with the free surface: Russel's wave generator

In this section, we address model validation for the more complex phase (ii) of water penetration, during which strong interactions occur between the slide and the free surface. Such penetration involves a highly dynamic force balance between slide weight, minus the time varying buoyancy force, and slide–fluid interaction forces, which strongly depend on free surface deformation. To validate the model in this case, we first compared simulation results to detailed experiments of Monaghan and Kos (2000), for a rectangular solid block falling vertically in the water. Such experiments qualitatively reproduce the "wave generator" described by Russel (1844), who witnessed the generation of a quasi-solitary wave in a shallow canal of constant depth, by a an abruptly stopping barge. The experiment was performed in a 9 m long 2D flume, with water depth D (Fig. 7). A 38.2 kg rectangular block (0.4 m tall, 0.3 m long and 0.39 m wide), placed just above still water level, was released at initial time $t = 0$. Experiments were repeated for $D = 0.288$, 0.210, and 0.116 m; in each case, the block vertical position and resulting free surface deformation were measured as a function of time (the latter at a wave gage located 1.2 m from the leftward extremity of the flume).

In experiments, the main flow feature caused by the falling block, is the development of a vortex at the block lower right corner; this is followed by the development of a small plunging breaker on the free surface, near the block right side. As time increases, the vortex detaches from the block and advects rightwards, while gradually losing strength. Fig. 8 shows corresponding simulations with the NS-PLIC model, in which, as in experiments, the block was forced to have a vertical motion by setting its horizontal velocity to zero, and was slightly shifted rightwards (by 25 mm). The model had a constant mesh size Δx_0 (resp. Δz_0 for $0 \le x \le 0.5$ (resp. $0 \le z \le 0.31$)) and then an exponentially increasing grid size over the rest of the domain, to $x = 9$ m. The following mesh sizes were tested: $\Delta x_0/L = \Delta z_0/L = 0.02$, 0.01 and 0.005, where L is block length. A free slip condition was specified along all solid boundaries. Block viscosity was set to 10^{10} Pa s, except for the finest mesh, for which accurate results could only be obtained using a smaller viscosity of 10^4 Pa s. Time step was set to 5.10^{-3} s for the first iterations and then automatically calculated so that the mesh Courant number was less than 0.3 after this.

Measurements of block velocity in Fig. 9 show an initial increase, from $t = 0$ to about $0.4\sqrt{(gD)}$ until the block has penetrated half the channel depth, followed by a decrease to 0.

Fig. 8, shows snapshots of streamlines and fluid interface locations, computed during the fall of the block. Within the block, streamlines are rectilinear, confirming that the penalty method truly yields a rigid body-like velocity field. Overall, the block geometry is well conserved during motion. As observed in Monaghan and Kos' (2000) experiments (as well as in their SPH simulations), a strong vortex is created at the lower right corner of the block during water penetration, which is then advected rightwards by the flow. Two large vortices are also generated during motion in the air at the block top corners. Snapshots of interfaces between water and air display the wave generation and initial stages of propagation. The first wave, which is the highest, is directly a function of the water volume displaced during block penetration. At $t = 0.28$ s (Fig. 8b), the simulated free surface shows a (backward) plunging breaker impacting the lower right part of the block; this was also observed by Monaghan and Kos in both their experiments and simulations. Note, the latter flow feature was quite difficult to accurately simulate using the methodology presented here. After various trials, we elected to solve Eq. (3) with the TVD scheme and Eq. (4) with the PLIC algorithm, using a small Courant Number of 0.3. The PLIC method is required for its accuracy in describing interface geometry, while the use of the TVD scheme results from practical stability reasons. In Fig. 8b, the plunging jet is seen to break up into small droplets, which is an unfortunate effect, because when such small water droplets travel with high velocity in the air, it becomes harder to accurately solve NS equations and, sometimes, computations might be even divergent. In particular, this is the case when using the PLIC algorithm to describe such droplets, while the TVD scheme smoothes out these features as a result of numerical diffusion in the direct solution of Eqs. (3) and (4).

The block velocity, simulated using the NS-PLIC and NS-TVD methods with coarse to fine meshes, is compared to Monaghan and Kos' (2000) experiments in Fig. 9. Intermediate mesh results are not

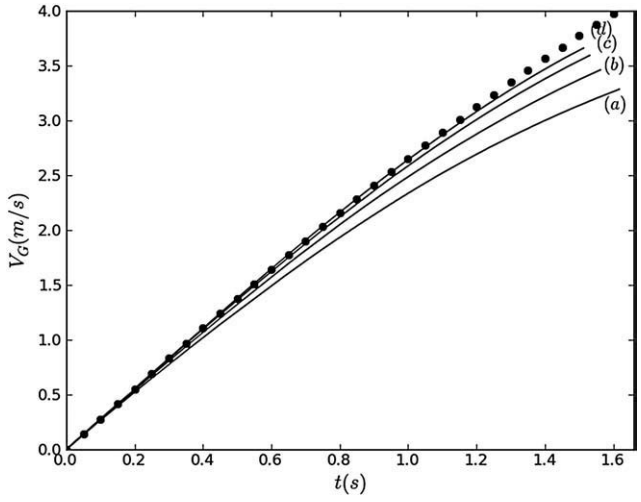

Fig. 6. Same case as Fig. 4 but using NS-PLIC model. (a) $\Delta x/L = 0.02$, (b) $\Delta x/L = 0.01$, (c) $\Delta x/L = 0.005$, and (d) $\Delta x/L = 0.003$.

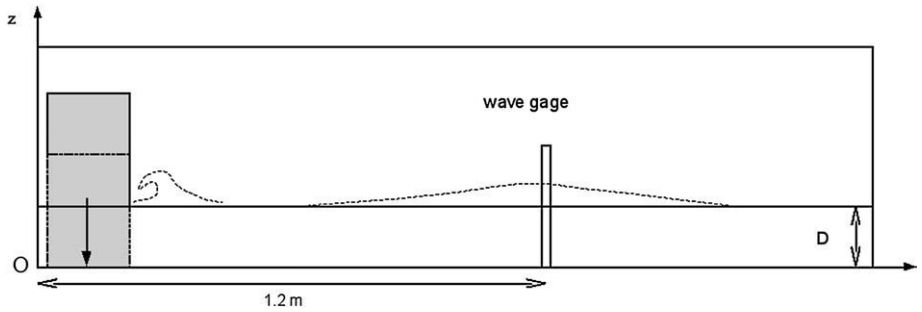

Fig. 7. Sketch of Russel's wave generator from Monaghan and Kos' (2000) experiments.

presented for sake of clarity, but these just fell within the other curves. Experimental error bars are also shown on the plot. Overall, simulation results agree well with measurements. The block velocity rapidly increases, until it reaches a maximum value of about 40% the long wave celerity, and then decreases to 0 when the block reaches the channel bottom. Monaghan and Kos reported oscillations of the simulated velocity, which were not well resolved in the measurements, due to the technique employed. We do not observe such oscillations in our simulations. When comparing the two interface tracking algorithms, we see NS-PLIC simulates a slightly slower block velocity than NS-TVD, with a maximum value of 0.407c for PLIC and 0.423c for TVD ($c = \sqrt{(gD)}$ being the wave celerity) using the finest mesh. For both methods, using a finer mesh leads to an increase in maximum velocity.

Table 1 shows a comparison of simulated and measured wave heights for three channel depths. Simulation results obtained using NS-PLIC and NS-TVD, are given for depth $D = 0.21$ m, for three meshes. For other depths, only results using NS-PLIC and the intermediate mesh size are reported. The accuracy of measured wave heights is about 10% for the three depth cases. Hence, the maximum error in simulations cannot be verified within less than 10% against experiments. Considering for instance the first result obtained with NS-PLIC in the coarsest grid, simulation results are within the experimental error bar. The maximum discrepancy of simulated to measured wave height is 17.8% and the minimum is 0%. Decreasing grid size in NS-PLIC simulations does not further improve accuracy; overall, results are comparable with NS-TVD, except that better results are obtained in the intermediate water case and worse results in the finer grid case. Simulations of other depth cases approximately lead to the same values of minimum and maximum discrepancies.

For the case $D = 0.21$ m, we also give values of H and B at $t = 0.28$ s as defined in Fig. 8. Here experimental measurements are more accurate and thus numerical results can be validated more precisely against these. In all cases, the measured H is reproduced by the model within at best 8% and at worst 14%. The discrepancy is larger for B, which was measured less accurately. This parameter is obtained with an accuracy varying between about 4 and 18%. We also note that Monaghan and Kos (2000) found very similar error values based on their SPH simulations.

3.3. Rigid triangular body sliding down an incline

3.3.1. 2D case — *Heinrich (1992) experiments*

Heinrich (1992) performed experiments, in which a triangular (0.5 m × 0.5 m) rigid block with a 105 kg mass freely slid down a 45° slope (Fig. 10). The water depth was 1 m and the top of the block was initially located 1 cm below the undisturbed free surface. Free surface displacements induced by the sliding block were measured as a function of time, using an optical camera. In the model, the physical domain is represented by an 8 m × 8 m square, in which gravity is inclined at 45° from vertical (Fig. 11). This particular configuration allows for easily setting the free slip boundary condition under the slide. The channel bottom is simulated as a porous medium, for which porosity tends to zero, thus imposing zero velocity for the fluid within

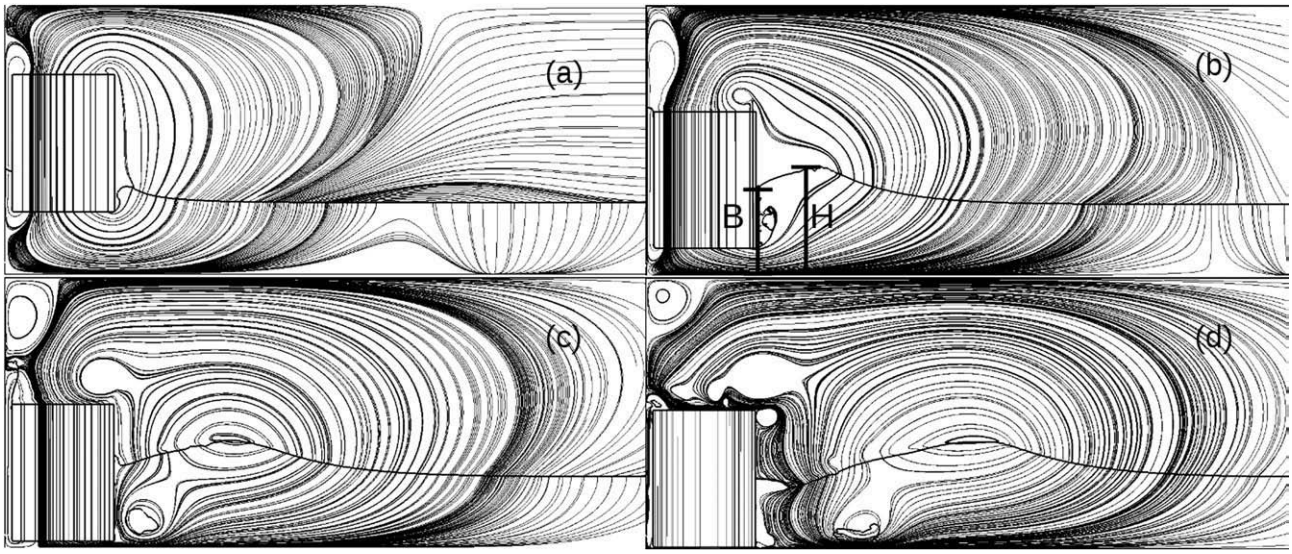

Fig. 8. Snapshots of NS-PLIC streamlines and fluid interfaces for the case of Fig. 7 at $t=$: (a) 0.1 s, (b) 0.28 s, (c) 0.42 s and (d) 0.61 s. Model grid size is $\Delta x_0/L = \Delta z_0/L = 0.01$.

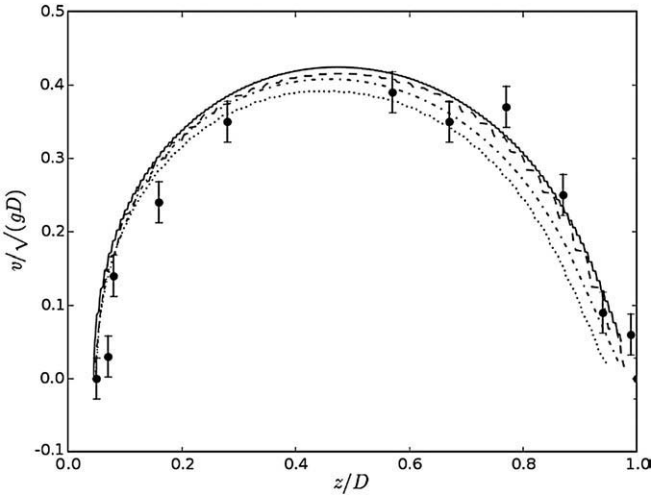

Fig. 9. Case of Fig. 7. Normalized vertical block velocity as a function of vertical location. (•): Monaghan and Kos (2000) experiments, (···) NS-PLIC $\Delta x_0/L=\Delta z_0/L=0.02$, (-·) NS-PLIC $\Delta x_0/L=\Delta z_0/L=0.005$, (--) NS-TVD $\Delta x_0/L=\Delta z_0/L=0.02$, (-) NS-TVD $\Delta x_0/L=\Delta z_0/L=0.005$.

it. The computational grid consists of regular cells, with $\Delta x'/L=\Delta z'/L=1.8\%$ ($L=0.707$ m), for $x'<5$ m and $z'<5$ m, exponentially increasing in size beyond those dimensions. Time step is set to 0.005 s for the first 50 iterations and then automatically computed using a maximum mesh Courant number of 0.5. Free slip boundary conditions are specified for the velocity components along all boundaries.

The slide is made rigid by specifying a large viscosity of 10^{10} Pa s. Interfaces are tracked using the TVD superbee method. Computations were also carried out using NS-PLIC for comparison, but wave breaking generated by slide motion induced the formation of small water droplets with high velocity, which heavily slowed down computations because of the CFL criterion. Nevertheless, results in terms of slide velocity and free surface deformation were very similar with both methods.

Table 1
Wave height and other free surface features. Comparison between Monaghan and Kos experimental values and model results. Experimental wave height values are reported with their relative accuracy in meter and percentage (in parenthesis).

	Monaghan and Kos (2000) experiment	NS-PLIC	NS-TVD
$D=0.21$ m		0.0966 ($\Delta x_0/L=0.02$)	0.0982 ($\Delta x_0/L=0.02$)
Wave height (m)	0.092 ± 0.01	0–17.8%	0–19.8%
Min and max	(10.9%)	0.1092 ($\Delta x_0/L=0.01$)	0.1058 ($\Delta x_0/L=0.01$)
errors in %		7–33%	3.7–29%
		0.1011 ($\Delta x_0/L=0.005$)	0.1065 ($\Delta x_0/L=0.005$)
		0–23%	4.4–29.9%
$D=0.288$ m		0.1024 ($\Delta x_0/L=0.01$)	
Wave height (m)	0.093 ± 0.01	0–23.4%	
Min and max	(10.7%)		
errors in %			
$D=0.116$ m		0.0967 ($\Delta x_0/L=0.01$)	
Wave height (m)	0.109 ± 0.01	2.3–18.7%	
Min and max	(9.17%)		
errors in %			
$D=0.21$ m		0.295 ($\Delta x_0/L=0.02$)	0.3 ($\Delta x_0/L=0.02$)
H (m)	0.333 ± 0.01	8.7–14%	7.1–12.5%
Min and max	(3%)	0.294 ($\Delta x_0/L=0.01$)	0.298 ($\Delta x_0/L=0.01$)
errors in %		9–14.3%	7.7–13.1%
		0.297 ($\Delta x_0/L=0.005$)	0.294 ($\Delta x_0/L=0.005$)
		8–13.4%	9–14.3%
$D=0.21$ m		0.264 ($\Delta x_0/L=0.02$)	0.264 ($\Delta x_0/L=0.02$)
B (m)	0.303 ± 0.02	6.7–18.3%	6.7–18.3%
Min and max	(6.6%)	0.27 ($\Delta x_0/L=0.01$)	0.27 ($\Delta x_0/L=0.01$)
errors in %		4.6–16.4%	4.6–16.4%
		0.272 ($\Delta x_0/L=0.005$)	0.27 ($\Delta x_0/L=0.005$)
		3.9–15.8%	4.6–16.4%

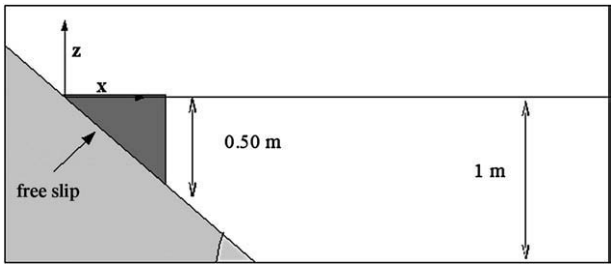

Fig. 10. Sketch of Heinrich's (1992) experiment for a solid triangular block sliding down an incline.

Fig. 12 displays a sequence of snapshots showing computed fluid interfaces and flow streamlines. The duration of slide motion is about 1 s, before the slide reaches the porous obstacle and stops (the lack of streamlines in the last two snapshots shows that the slide motion has effectively stopped). Overall, slide rigidity is well achieved, except at slide corners where small local deformations are observed. An elevation wave is created by the water displacement induced by the slide. Its crest is clearly visible at $t=1$ s, at the center of a streamline cell in the right half of the domain. A second wave is then generated over the slope, in the run-up region. The trough between the first and second waves is also visible at $t=1$ s. The second wave breaks between $t=1$ s and 1.5 s, leading to a fairly irregular free surface in this zone and to the generation of two small vortices under the wave. Then, the wave keeps propagating rightwards. A large vortex is also created at the right corner of the slide during motion, which then interacts with the vortices induced by wave breaking (Fig. 12d).

Numerical results are compared to Heinrich's experiments in Figs. 13 and 14. Fig. 13 compares the simulated and measured vertical displacements of the slide center of mass. Overall, the agreement is quite good with a RMS difference of 9.6 10^{-3} m. Fig. 14a,b compares computed and (digitized) experimental free surfaces, at respectively $t=0.5$ and 1 s. We see that the model reproduces well the overall behavior of the free surface displacement during the block sliding. In the propagation region (rightward part of the domain), the agreement between computed and measured free surfaces is seen to be very good. Main discrepancies appear near the slide, in the wave generation region. This was already the case in earlier numerical work attempting to simulate these experiments (Heinrich, 1992; Yuk et al., 2006). Let us also note that the use of coarser meshes, such as $\Delta x'/L=\Delta z'/L=3.6\%$ or even 7.2% is sufficient to achieve accurate results.

3.3.2. 3D case — *Liu et al. (2005) experiments*

Wu (2004) and Liu et al. (2005) carried out experiments in a large scale flume to study the wave field and subsequent run-up generated by a sliding three-dimensional rigid wedge. These experiments were also selected as a benchmark for numerical models, as part of the 3rd international workshop on long wave run-up models (Catalina, June 2004) as well as within the European project TRANSFER (Tsunami Risk And Strategies For the European Region). Fig. 15 shows a sketch of the experimental setup. Free surface elevation and run-up were measured at different locations, close to the generation area. Slide time evolution was also provided.

Liu et al. (2005), performed 3D-LES simulations, using the PLIC VOF method, and compared numerical results to their experimental data. They prescribed the slide motion in the model, based on the measured slide displacement, with the slide being close to the free surface at initial time. Upon slide release, free surface deformation is

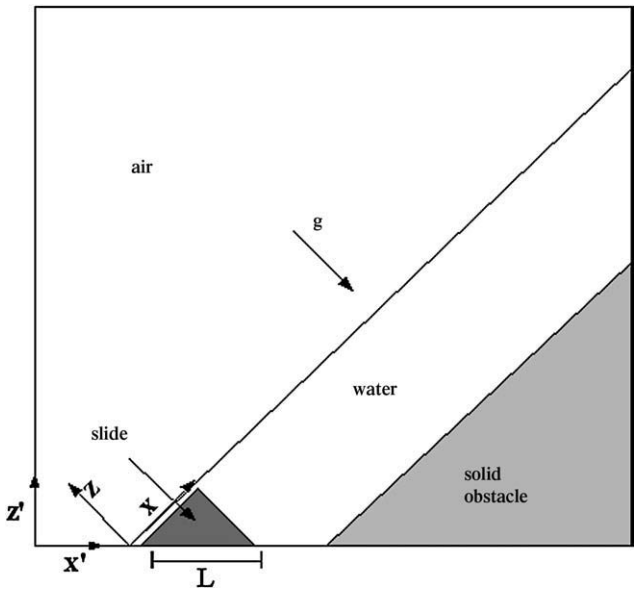

Fig. 11. Sketch of the domain used in the computations for case of Fig. 10.

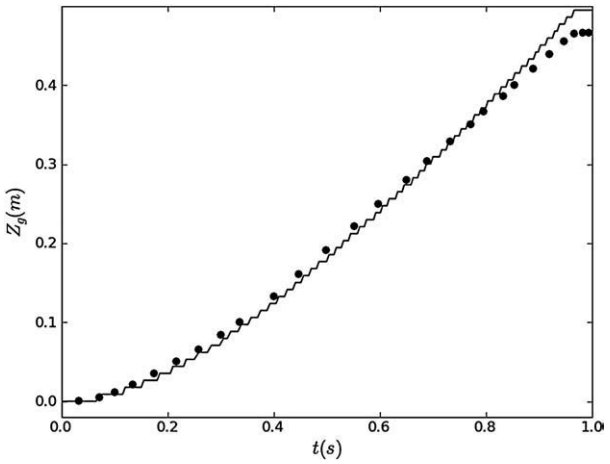

Fig. 13. Case of Fig. 10. Time evolution of vertical slide displacement. (•): Heinrich's (1992) experiments, (−): NS-TVD model simulations for a single rigid triangular block.

strong and wave breaking is susceptible to occur in certain cases. Complex flow patterns occur in all cases.

In this work, we simulated Liu et al.'s cases corresponding to different submergence values but, instead of prescribing slide motion, we solved for the coupling between slide and water. As in earlier applications, the rigid wedge was modeled as a Newtonian fluid of large viscosity (10^5 Pa s).

Here, we present in detail a case corresponding to one of the benchmark cases in which the slide initial emergence is $\Delta = -0.1$ m and slide density is 2.14. Like in the preceding section, x' is in the slope direction, z' is perpendicular to the slope plane (gravity being in this case inclined by 26.56° with respect to z'), $y = y'$ is the longshore direction. Due to symmetry with respect to the middle vertical plane, the computational domain is half the experimental flume (including run-up gage 1 and wave gage 1). Two numerical grids were tested to assess discretization effects on slide motion and subsequently on free surface deformation. Both grids were irregularly distributed over x' and z' to account for the need for finer resolution close to the generation zone. The first grid (mesh 1 with $62 \times 76 \times 24$ cells) is comparable to the mesh used in Liu et al. (2005). The finest grid cell size is $\Delta x' = 0.039$, $\Delta z' = 0.0196$, $\Delta y'$ being constant and equal to 0.077. For the second mesh used (mesh 2 with $170 \times 100 \times 120$ cells), the finest grid cell size is $\Delta x' = \Delta z' = 0.015$, $\Delta y'$ was constant and also equal to 0.015. Non-dimensional finest grid sizes are respectively $\Delta x'/L = \Delta z'/L = 3.8\%$ for mesh 1 and 1.4% for mesh 2 (with $L = 1.017$ m). High resolution 3D computations are very time consuming and parallelization of our model was required to keep computing times within reasonable bounds. For example, computations for the finest mesh take around 4 days to run on 8 processors (quadricore 3 GHz) for 5000 iterations. Before the parallelization of the model, such computations would last four times longer.

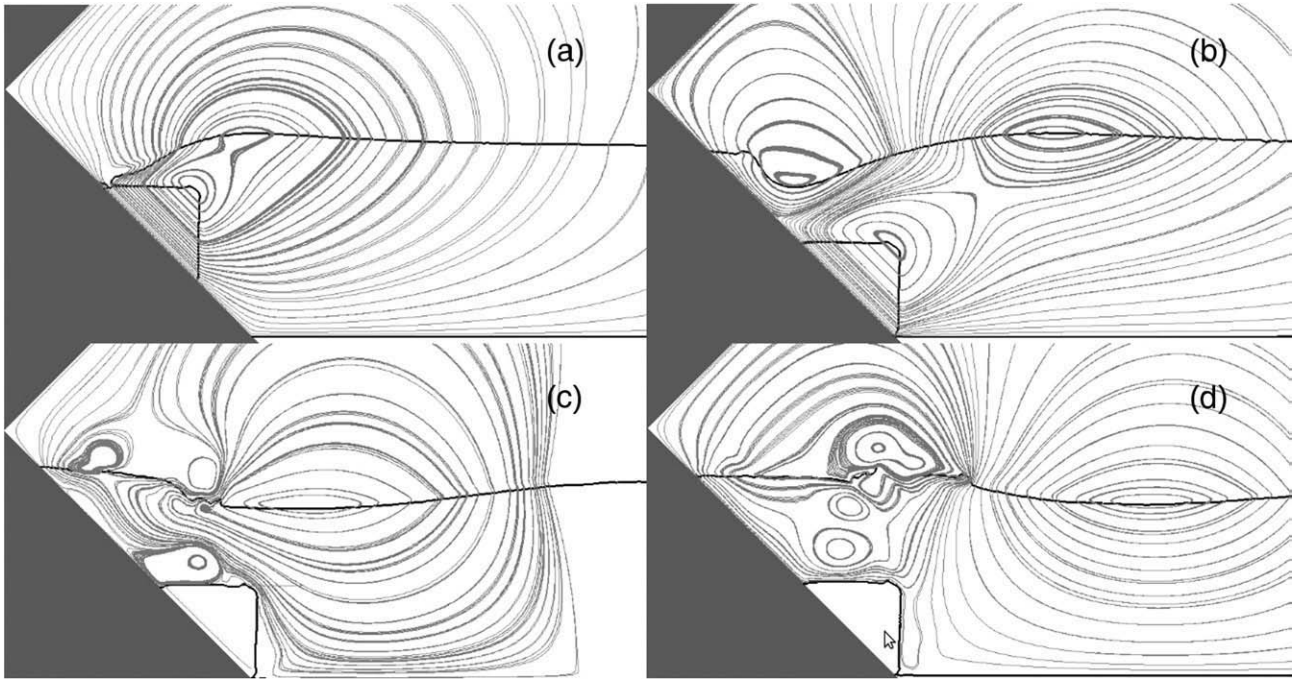

Fig. 12. Snapshots of fluid interfaces and flow streamlines in the case of Fig. 10, for a rigid slide ($\mu = 10^{10}$ Pa s) and using NS-TVD model at $t =$: (a) 0.5 s, (b) 1 s, (c) 1.5 s, and (d) 2 s.

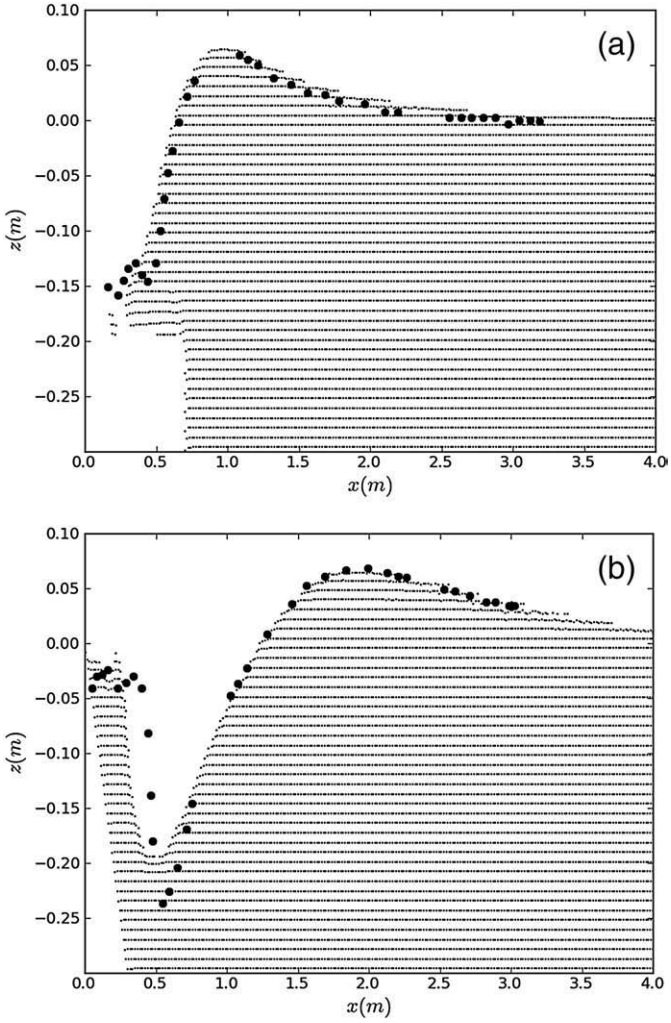

Fig. 14. Case of Fig. 10. Free surface deformation at $t=0.5$ s and $t=1$ s. (•): Heinrich's (1992) experiments, dot filled contour: NS-TVD model simulations using a single rigid triangular block. (a) $t=0.5$ s, and (b) $t=1$ s.

Fig. 16 shows snapshots of water/air and slide/water interfaces computed at four different time steps for the finest mesh, using the NS-PLIC model. In the last image at $t=3.5$ s, the slide has stopped on the horizontal bottom of the experimental flume, which is represented in simulations but not visible in Fig. 16. In this snapshot sequence, we observe the generation of a wave train, and its subsequent propagation and reflection from the vertical sidewalls of the flume. Maximum run-up, which occurs at the plan of symmetry on the flume axis, is seen to also propagate towards and reflect of the sidewalls.

Fig. 17 shows the simulated slide center of mass motion as a function of time compared to experimental data. The measured slide motion is well reproduced in the finer mesh grid with RMS deviation of 0.16 m. In the coarser grid, the slide is much slower than in experiments (larger RMS deviation of 0.80 m). A computation performed using an intermediate grid size (not presented here) yields a slide motion curve in between the two presented curves, indicating a consistent behavior of the model. Other computations for different initial submergence values also matched experimental data well, provided that a fine enough grid (i.e., with $\Delta x/L\sim 1\%$) is used. A closer inspection of our results indicates that, resolving the coupling between slide motion and water flow in the numerical model is achievable with good accuracy, but requires an overall grid about 20 times larger than when slide motion is *a priori* specified, as in Liu et al. (2005).

Fig. 18 compares surface elevations simulated at wave gages 1 and 2, both in the generation area (see Fig. 15), to experimental data. At gage 1, both the first elevation wave and through are well modeled in the finer grid 2, whereas the second wave is much higher (162%) than measured. This was also observed by Wu (2004) for this gage location and a slide initial submergence $D=-0.05$. Both waves phase and hence celerity, however, are correctly predicted in the finer grid 2, whereas the second wave is too slow in the coarser grid 1. Note that wave heights are also under-predicted in the latter grid, which is consistent with a slower slide (see Fig. 17). At gage 2, the lateral spreading of the wave (run-up) is also well simulated using grid 2; the simulated wave elevations are close to the experimental results, even though waves seem to be a bit slower. In grid 1 again, the slower slide generates both smaller and slower waves as compared to experimental data.

Fig. 19, similarly, compares run-up simulated at run-up gages 2 and 3 (see Fig. 15) to experimental data. At gage 2, in the finer grid, numerical results closely match experiments, except during the first run-up phase where the model overestimates the recorded run-up value and generates a quicker run-up motion. In the coarser grid, run-down and run-up values are both overestimated. A similar behavior is observed at gage 3. Wu (2004) also reported such discrepancies between run-up data and numerical result with an initial submergence $\Delta=-0.05$.

4. Discussion and perspectives

The few experimental validation cases presented above demonstrate our 3D-NS-VOF model's ability to accurately simulate the coupling between rigid slide motion and induced water flows and free surface deformation. As pointed out before, rigid slide cases are the most documented in the literature. Hence, a careful model validation process should logically start with this class of problems.

Although rigid slides are idealized as compared to actual slides, at this stage of validation, the numerical model can already provide useful information of potential practical interest. Specifically, as a validated numerical wave tank, our model can be used to replace or complement physical experiments (for rigid slide cases). Furthermore, our ability to correctly simulate slide motion, rather than specifying it in computations based on experimental measurements, implies that no preliminary experimental study is necessary for calculating slide motion. The accurate simulation of slide/water flow coupling could also help better understanding the phenomenon of landslide tsunami, through an analysis of energy and momentum exchanges between slide and water. This aspect could be investigated in detail in future numerical work, and energy exchange effects on slide law of motion and free surface deformation could be elucidated.

To illustrate the model's potential for simulating more realistic slides such as occurring in nature, in the following, we report on preliminary simulations for: (i) retrogressive slope failure; (ii) deformable slides; and (iii) rock slides akin to granular flows.

4.1. Retrogressive slope failure

Field work shows that, often, landslide tsunamis are created by processes involving several slides, potentially interacting with each other; this is referred to as retrogressive slope failure (e.g., Lovholt et al., 2005). In such cases, the motion of an individual slide may be strongly dependent upon the flow field generated by other preceding slides; hence, slide law of motion should be computed in a fully coupled way.

Preliminary simulations, similar to Heinrich's (1992) case (see Section 3.3.1) were performed to illustrate the model's ability to simulate multiple interacting slides. We considered the scenario of a slide occurring in two stages, in which Heinrich's triangular sliding block is broken up into two symmetrical rigid blocks initially

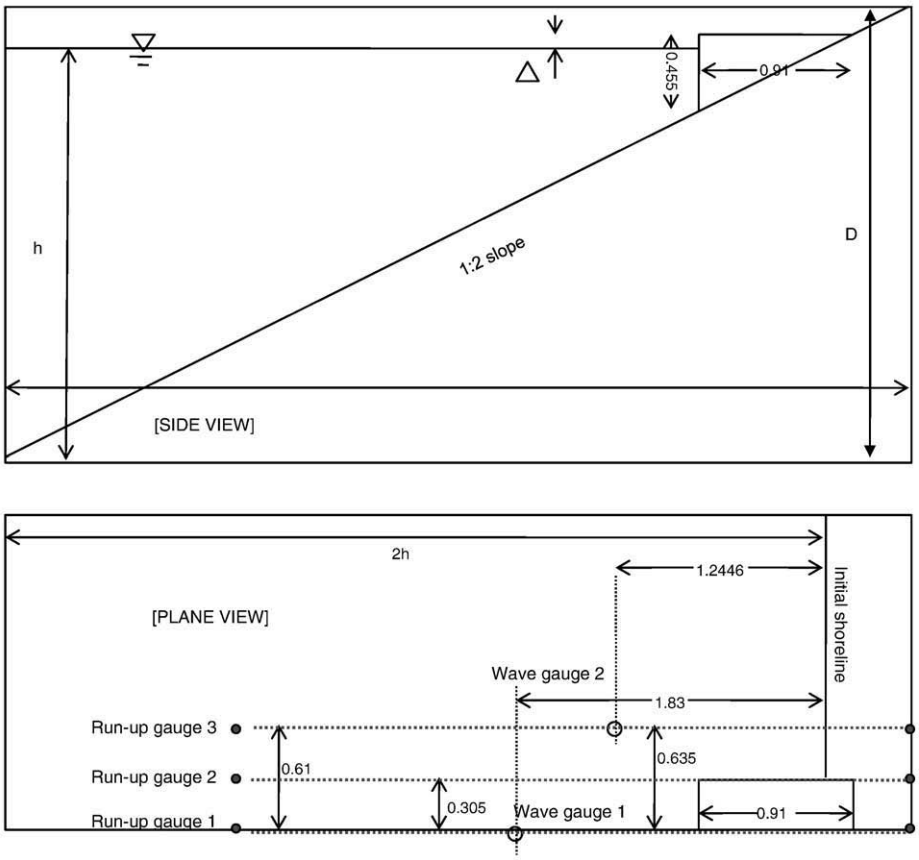

Fig. 15. Sketch of Liu et al. (2005) experiments (from the 3rd international workshop on long wave run-up models (Catalina, June 2004)).

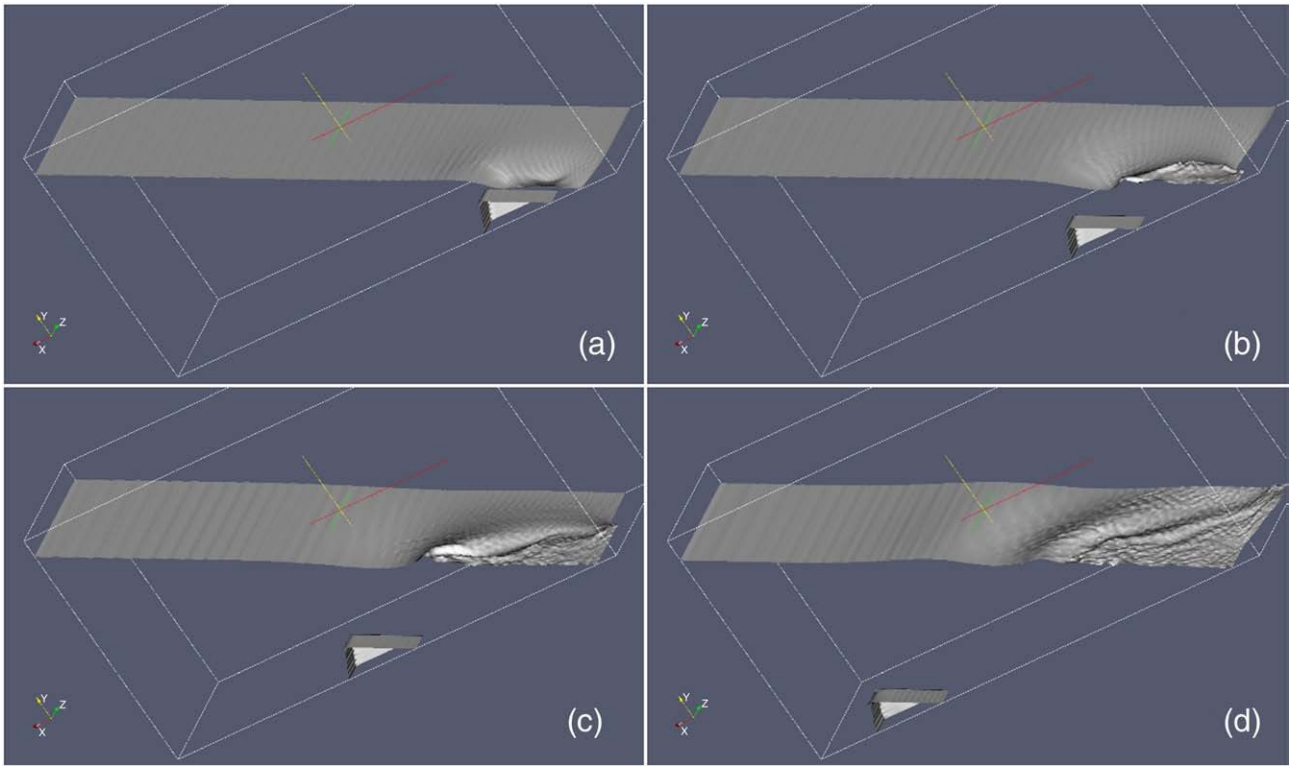

Fig. 16. Case of Fig. 15. Snapshots of slide/water and water/air interfaces at different times for grid 2 with $170\times100\times120$ cells. Slide initial submergence is $D=-0.1$ m, slide density is 2.14. (a) $t=0.7$ s, (b) $t=1.4$ s, (c) $t=2.1$ s, and (d) $t=3.5$ s.

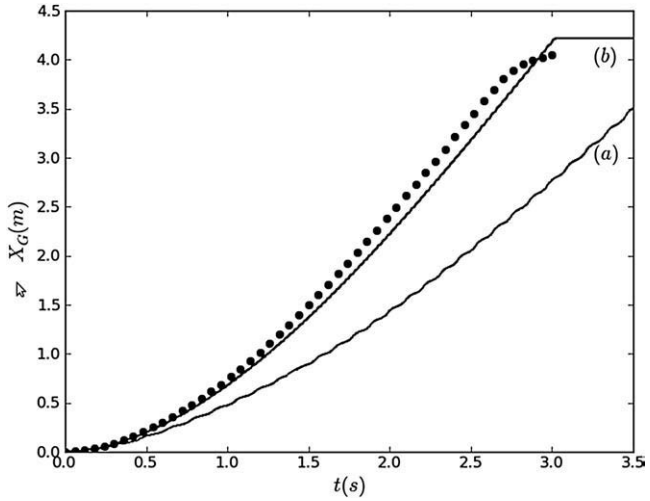

Fig. 17. Case of Fig. 15. Time evolution of slide center of mass. Solid lines: numerical results with (a) $62\times76\times24$ cells and (b) $170\times100\times120$ cells; (•): experimental data. Initial slide submergence is $\Delta=-0.1$ m, slide density is 2.14.

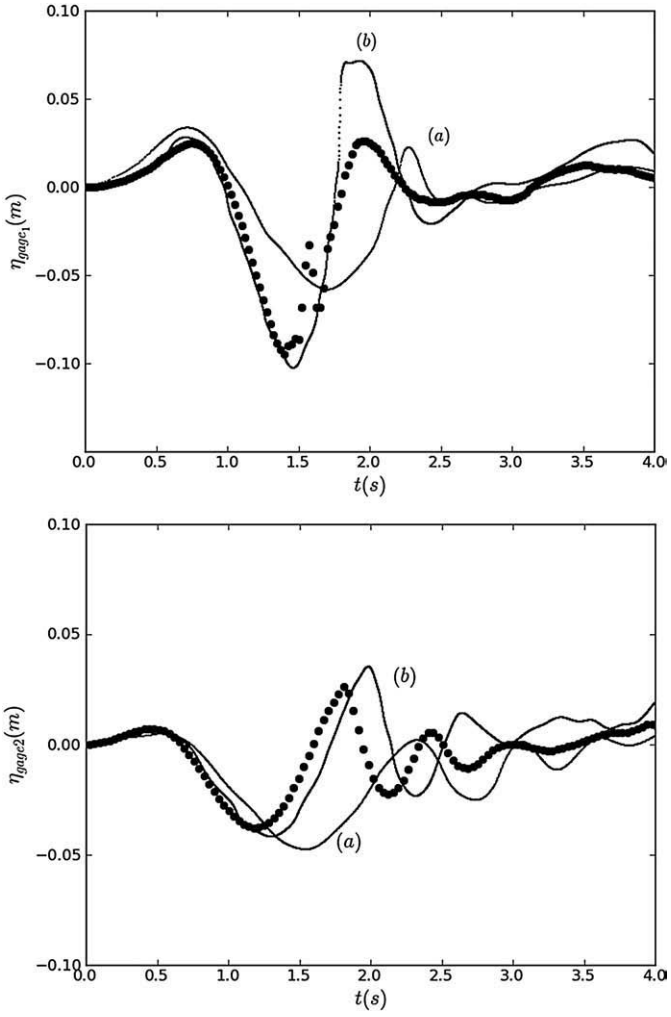

Fig. 18. Case of Fig. 15. Comparison between numerical results (solid lines) and experimental data (•) for the time histories of free surface elevations at wave gage 1 (top figure) and wave gage 2 (bottom figure). Initial slide submergence is $\Delta=-0.1$ m, slide density is 2.14. (a) $62\times76\times24$ cells, (b) $170\times100\times120$ cells.

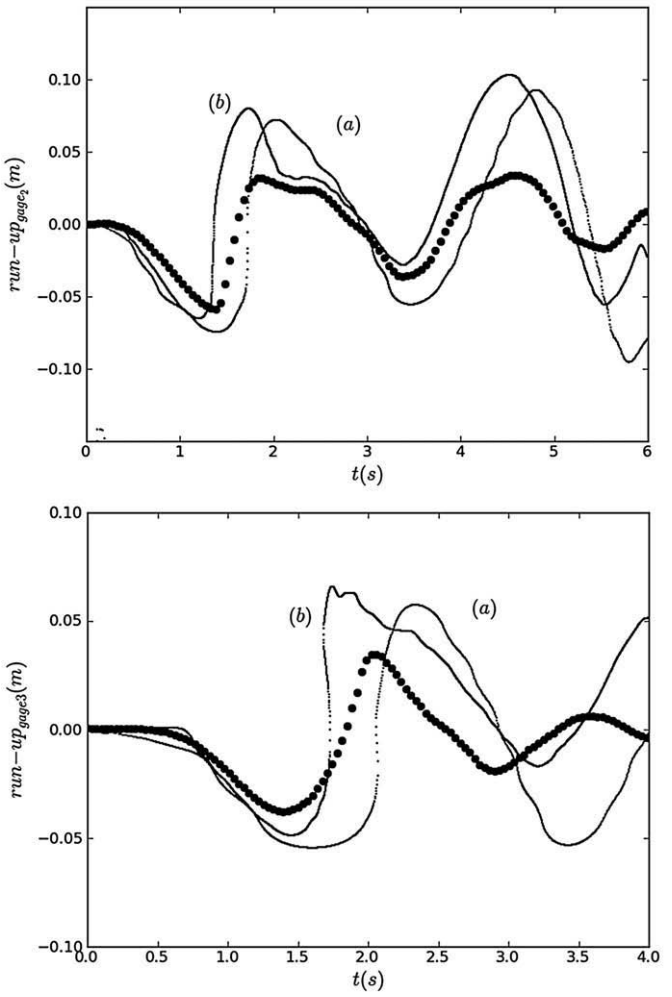

Fig. 19. Case of Fig. 15. Comparison between numerical results (solid lines) and experimental data (•) for the time histories of run-up at gage 2 (top figure) and gage 3 (bottom figure). Initial submergence is $\Delta=-0.1$ m, slide density is 2.14. (a) $62\times76\times24$ cells, and (b) $170\times100\times120$ cells.

separated by 3.5 cm (Fig. 20). Both blocks have physical properties identical to those of the Heinrich's case. In simulations, the bottom block is first released at $t=0$, while the upper block is forced to stay at rest by directly specifying zero fluid velocities within the discretized matrix. At $t=1$ s, the upper block is released by relaxing the constraint on fluid velocity.

Fig. 20 shows snapshots of fluid interfaces computed for this scenario. At $t=0.5$ s, water has flown within the gap between the blocks, which is opening up. The second block/slide motion is initiated at $t=1$ s (as illustrated by streamlines shown on the second snapshot of Fig. 20). At this time, we observe an almost flat free surface at the scale of the figure, indicating that only a tiny wave is generated by the first block motion, due to its deep submergence and smaller volume as compared to the single slide scenario (Fig. 12). Once the second shallower block/slide motion is initiated, the free surface deformation becomes much larger, with a time sequence similar to that of the single block case.

4.2. Deformable slides

Although this is outside the scope of this paper, to illustrate the model's ability to simulate slide deformation during motion, and its effect on wave generation, we performed preliminary simulations for the case of a deformable slide, similar to that of Fig. 10. We used the same density as in the rigid case, but a much lower viscosity of 10^2 Pa s. For this case, Fig. 21 shows that, as soon as the slide starts

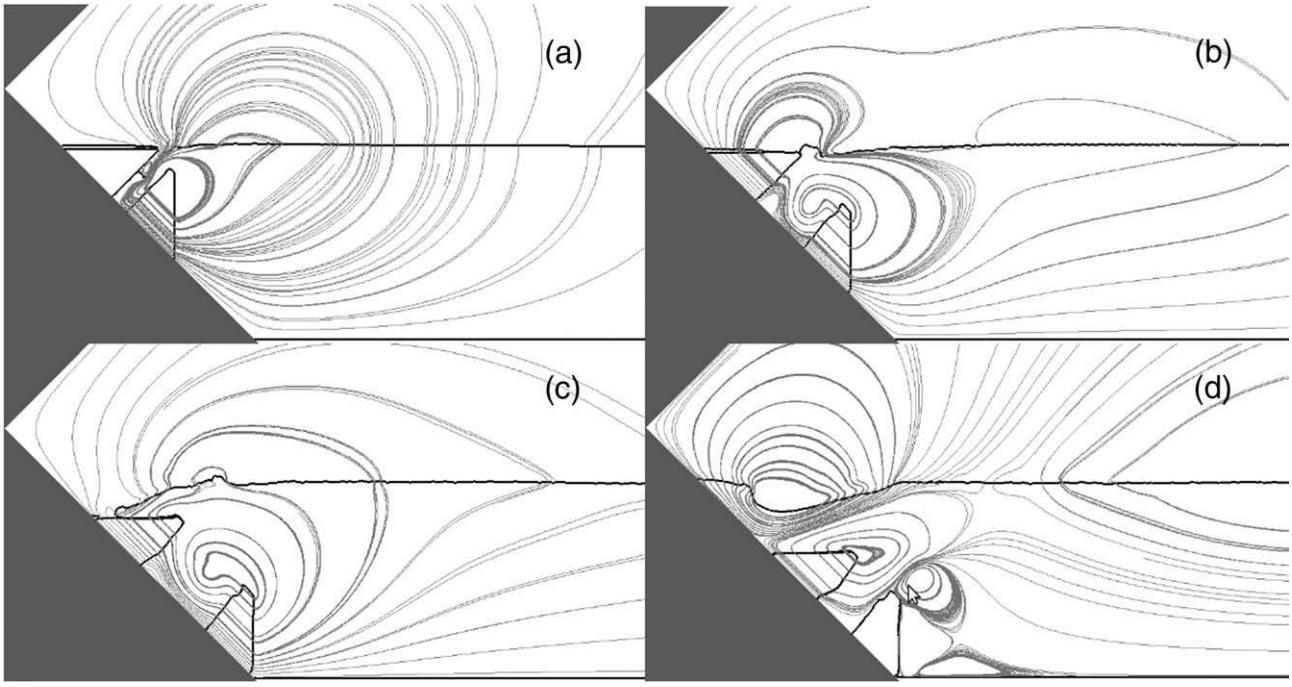

Fig. 20. Two-rigid slides scenario (1 s delay). Snapshots of fluid interfaces and flow streamlines. Slide viscosity $\mu = 10^{10}$ Pa s at $t =$ (a) 0.5 s, (b) 1 s, (c) 1.5 s, and (d) 2 s.

moving, it loses its initial shape and becomes thinner with a bulbous front ($t = 0.5$ s). At $t = 1$ s, 1.5 s and 2 s, the slide moves over the porous medium on the bottom, and progressively slows down due to the zero velocity condition, which is implicitly imposed on the slide by this medium.

The induced free surface elevation is qualitatively similar to that of the rigid case, with the generation of two consecutive waves. However, the second wave is less steep than for the rigid case, due to the thinning of slide geometry, and hence does not immediately break. This results in reduced dissipation and, consequently, at $t = 2$ s the wave seems higher than in the rigid case.

While, based on these results, the model is clearly able to simulate deformable slides, the idealized simulations of Fig. 21 raise the question of validation. First of all, real slides are complex phenomena whose behavior depends on soil type as well as environmental and geometrical parameters (Varnes, 1978). This complexity must be taken into account in the model, in particular, by using a relevant rheological law. So far, Newtonian and visco-plastic laws (i.e. Herschel–Bulkley fluid) have been implemented and used in the model. Such simple laws, however, may only be suited to represent a small class of slides, which are nearly or fully saturated (Quecedo et al., 2004).

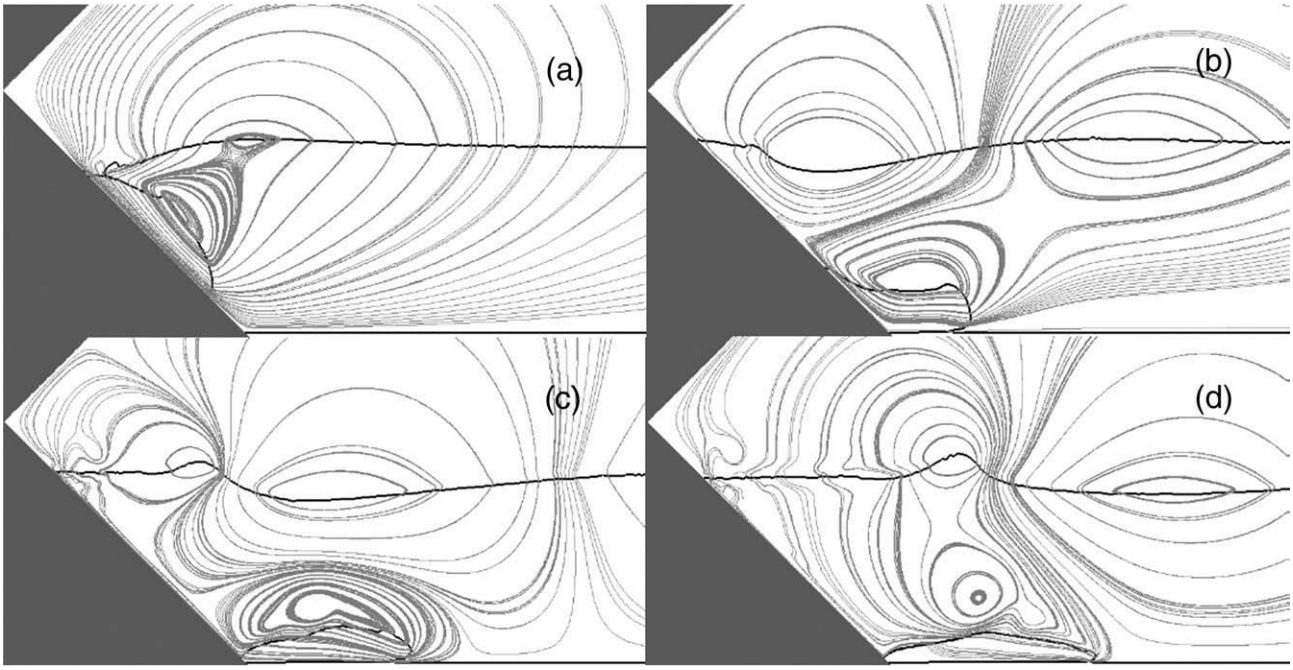

Fig. 21. Same as in Fig. 21 with a deformable slide ($\mu = 10^2$ Pa s).

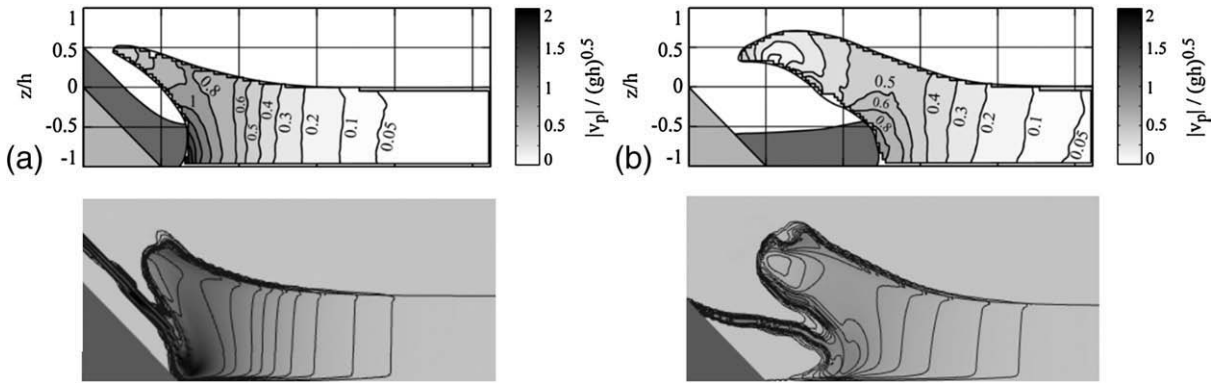

Fig. 22. Simulations of Fritz (2002) 2D granular slide experiments (top figures), as a Newtonian fluid (bottom figures), with water depth $h = 0.3$ m, slide density is 2.64, slide volume $V = Vs/bh^2 = 0.79$ (with b channel width), slide thickness $S = s/h = 0.34$, and impact Froude number $F = 2.8$. Figures are given at time $t / \sqrt{(g/h)}$=: a) 0.72, and b) 1.48.

4.3. Rock slides and granular flows

Rock slides may be represented as granular flows, for instance using the macroscopic formulation given in Chen and Ling (1996). To date, however, 3D simulations of tsunamis caused by rock slides have only been performed using simpler rheological laws (e.g., a Newtonian law as in Abadie et al., 2009, or a Bigham law as in Gisler et al., 2006). The main difficulty for performing realistic simulations of deformable slides of any type, is the paucity of detailed and relevant experimental results that could be used for validation.

In this respect, Fritz (2002) and more recently Heller et al. (2008) are among the very few studies to have reported comprehensive experiments of waves generated by granular subaerial slides. In Fritz's 2D experiments, slide kinematics was obtained from laser measurements and the flow kinematics was investigated in the generation zone, using a Particle Image Velocimetry (PIV) method.

To assess the model's ability to simulate granular flows as Newtonian slides, for high impact Froude numbers F (defined as $F = V_s / \sqrt{(gh)}$, where V_s is the slide impact velocity), we simulated a few of the cases reported by Fritz (2002). One case is presented in Fig. 22, with water depth $h = 0.3$ m, slide density 2.64, slide volume $V = V_s/bh^2 = 0.79$ (with b channel width), slide thickness $S = s/h = 0.34$, and impact Froude number $F = 2.8$. Fritz made laser measurements of slide free surface at 0.07 m from the water line. We used these measurements to specify the initial slide geometry in the numerical model; doing so, the slide was initially located so that the slide tip corresponds to the water line. Slide initial velocity was set to 4.80 m/s, in accordance with $F = 2.8$. Like in Heinrich's case and for the same reason, gravity was inclined at $-45°$ and the x direction of the computational domain corresponds to the slope. The computational grid consisted in irregular cells, with the finest mesh size being $\Delta x'/L = \Delta z'/L = 1.8\%$.

The time step was automatically computed to achieve a mesh Courant number less than 0.2, because slide motion is quite violent in this case, leading to high rates of water/air interface deformation. Several simulations were carried out, using different slide Reynolds numbers Re_s (defined as $\rho_s v_s s/\mu_s$). Slide viscosity was tuned so that the first simulated wave fits experimental data at best, at the specified time. The best results were obtained using $Re_s = 5.2$ (i.e. $\mu = 150$ Pa s), which are shown in Fig. 22 together with Fritz's experimental results, for free surface deformations and water velocity values at two different times during the generation process. The agreement is quite good, even though some differences in slide and free surface geometry can be observed. A large air volume is subsequently entrapped at the back, during slide motion, stressing the importance of also modeling air flow for such high impact Froude cases. [Note that the model provides other important parameters (e.g., slide velocity and water pressure), which were not measured in experiments, due to practical difficulties.]

A closer inspection of numerical results indicates that, while the first wave time evolution (not shown here) is well simulated in Fig. 22, the model does not reproduce trailing waves so well as compared to experimental data. Moreover, both the initial and subsequent wave generation processes are found to be very dependent on slide Reynolds number (Morichon and Abadie, 2010). Finally, the optimal slide Reynolds number found for this case does not seem to be universal and may vary with the impact Froude number.

In closing, this preliminary investigation of more complex types of slides indicates that, although progress has been made, this problem is still far from being satisfactorily solved, which in particular stresses the need for a careful and thorough model validation process.

5. Conclusions

A model solving Navier–Stokes equations for three fluids (water, air and slide), with a Volume of Fluid (VOF) algorithms to track fluid interfaces has been applied to the problem of waves generation by landslides. Deformable slides are simulated as Newtonian (or non-Newtonian) fluids. A penalty method is used to simulate rigid slides. In this new formulation of the problem, we fully model the coupling between slide and water during motion. To validate the model, simulation results were compared to semi-empirical laws of motion and experimental data. The following conclusions can be drawn:

- Direct numerical simulations of Navier–Stokes equations allow us to accurately simulate impulse waves generated by subaerial or submarine rigid slides, from generation to propagation stages.
- The penalty method used in the model efficiently simulates solid/fluid interactions, and allows to accurately model rigid slide motion as a fluid. With this method, it is now possible to directly calculate slide motion (rather than specifying it as a boundary condition) and generated waves, without requiring any further experimental studies as in numerical work published earlier on this topic.
- The aerial phase of rigid slide motion is very accurately simulated in the model. The submarine phase is more complex. Simulations carried out considering semi-elliptical shapes show that the use of a fine mesh and an accurate VOF method such as PLIC is required to reproduce the correct slide law of motion underwater. Other simulations considering wedges are less sensitive to mesh size or the choice of VOF algorithm.
- The ability of the model to properly simulate the penetration of a solid in water was assessed by comparing numerical results with the 2D experiments (and SPH simulations) of Monaghan and Kos (2000). The block kinematics was well reproduced and free surface elevations matched experimental results reasonably well.
- The model was successfully applied to a 3D slide, by comparing to experimental and other numerical results (Liu et al., 2005). In our case, due to the full modeling of slide/water interactions, the

numerical grid required to obtain good accuracy was 20 times that used in Liu et al. (2005), based on a specified slide motion. Such demanding computations required using a parallel version of the model.

- Other preliminary simulations were run, that illustrated the model's ability and potential for simulating more complex and realistic slide cases such as: (i) retrogressive slope failure; (ii) deformable slides; and (iii) rock/granular flows.

Based on the above 2D and 3D validation cases, we conclude that the 3D-NS-VOF model can be used as a useful validated tool, for performing both fundamental investigations (e.g., slide/water energetic exchanges) and more practical simulations (e.g., retrogressive rigid slides) of landslide wave generation. Regarding deformable slides, because of the complexity and diversity of real slides, as well as the lack of data available for comparison, the process of validation, initiated here, should be pursued as a long-term goal, by simulating experimental benchmark cases, as they become available.

Acknowledgments

This work was supported by a grant from the "Tsunami Risk and Strategies for the European Region" program, funded by the European Commission, under contract no. 037058. Partial support for Stephan Grilli was provided by grant no. EAR-0911499 of the NSF Geophysics Program. The authors also wish to gratefully acknowledge the "Aquitaine Regional Council" for supporting the acquisition of a 256- processor cluster, located in the TREFLE laboratory.

References

Abadie, S., Caltagirone, J.P., Watremez, P., 1998. Splash-up generation in a plunging breaker. CRAS — Ser. IIB — Mech. Phys. Astron. 326 (9), 553–559.
Abadie, S., Gandon, C., Grilli, S., Fabre, R., Riss, J., Tric, E., Morichon, D., Glockner, S., 2009. 3D numerical simulations of waves generated by subaerial mass failures. Application to La Palma case 2009. In: Mc Kee Smith, J. (Ed.), Proc. 31st Intl. Coastal Engng. Conf. Hamburg, Germany, pp. 1,384–1,395. ICCE08, September, 2008.
Amestoy, P.R., Duff, I.S., L'Excellent, J., 2000. Multifrontal parallel distributed symmetric and unsymmetric solvers. Comput. Methods Appl. Mech. Eng. 184, 501–520.
Assier Rzadkiewicz, S., Mariotti, C., Heinrich, P., 1997. Numerical simulation of submarine landslides and their hydraulic effects. J. Waterw. Port Coast. Ocean Eng. 123 (4), 149–157.
Breil J., Caltagirone J.P., 2000. Three dimensional computer simulation of mould filling with N fluids by VOF PLIC and projection methods, ICCFD, Kyoto, July 10–14.
Chen, C., Ling, C., 1996. Granular-flow rheology: role of shear-rate number in transition regime. J. Eng. Mech. (ASCE) 122, 469–480.
Enet, F., Grilli, S.T., Watts, P., 2003. Laboratory Experiments for Tsunamis Generated by Underwater Landslides: Comparison with Numerical Modeling. In Proc. 13th Offshore and Polar Engng. Conf. (ISOPE03, Honolulu, USA, May 2003), pp. 372–379.
Enet, F., Grilli, S.T., 2005. Tsunami landslide generation: modelling and experiments. Proc. 5th Intl. on Ocean Wave Measurement and Analysis (WAVES 2005, Madrid, Spain, July 2005). IAHR Publication. paper 88, 10 pps.
Enet, F., Grilli, S.T., 2007. Experimental study of tsunami generation by three-dimensional rigid underwater landslides. J. Waterw. Port Coast. Ocean Eng. 133 (6), 442–454.
Fortin, M., Glowinski, R., 1982. Méthodes de lagrangien augmenté. Application à la résolution numérique de problèmes aux limites, Dunod, Paris.
Fritz H.M., 2002. Initial phase of landslide generated impulse waves. Thesis Versuchsanstalt für Wasserbau, Hydrologie und Glaziologie, ETH Zürich, Swiss ETH No. 14'871. Swiss Federal Inst. Techn., Zürich, ISSN 0374-0056.
Fritz, H.M., Hager, W.H., Minor, H.E., 2001. Lituya Bay case: rockslide impact and wave run-up. Sci. Tsunami Hazards 19 (1), 3–22.
Fritz, H.M., Hager, W.H., Minor, H.E., 2004. Near field characteristics of landslide generated impulse waves. J. Waterw. Port Coast. Ocean Eng. 130 (6), 287–302.
Gisler, G., Weaver, R., Gittings, M.L., 2006. Sage calculations of the tsunami threat from La Palma. Sci. Tsunami Hazards 24 (4), 288–301.
Grilli, S.T., Watts, P., 1999. Modeling of waves generated by a moving submerged body. Applications to underwater landslides. Eng. Anal. Bound. Elem. 23, 645–656.
Grilli, S.T., Watts, P., 2005. Tsunami generation by submarine mass failure Part I: modeling, experimental validation, and sensitivity analysis. J. Waterw. Port Coast. Ocean Eng. 131 (6), 283–297.
Grilli, S.T., Vogelmann, S., Watts, P., 2002. Development of a 3D numerical wave tank for modeling tsunami generation by underwater landslides. Eng. Anal. Bound. Elem. 26 (4), 301–313.
Grilli, S.T., Taylor, O.-D.S., Baxter, D.P., Maretzki, S., 2009. Probabilistic approach for determining submarine landslide tsunami hazard along the upper East Coast of the United States. Mar. Geol. 264 (1–2), 74–97. doi:10.1016/j.margeo.2009.02.010.
Grilli, S.T., Dias, F., Guyenne, P., Fochesato, C., Enet, F., 2010. Progress in fully nonlinear potential flow modeling of 3D extreme ocean waves. Chapter in Advances in Numerical Simulation of Nonlinear Water Waves (Series in Advances in Coastal and Ocean Engineering Vol. 11, ISBN: 978-981-283-649-6). World Scientific Publishing Co. Pte. Ltd., 55 pps.
Gumusel, B., Kavurmacioglu, L., Camci, C., 2006. Aerodynamic drag characteristics and shape design of a radar antenna used for airport ground traffic control. Proceedings of the International Symposium on Transport Phenomena and Dynamics of Rotating Machinery. Honolulu, Hawaii, USA.
Harbitz, C.B., 1992. Model simulations of tsunamis generated by the Storegga slides. Mar. Geol. 105, 1–21.
Haugen, K.B., Løvholt, F., Harbitz, C.B., 2005. Fundamental mechanisms for tsunami generation by submarine mass flows in idealised geometries. Mar. Pet. Geol. 22, 209–217.
Heinrich, P., 1992. Non linear water waves generated by submarine and aerial landslides. J. Waterw. Port Coast. Ocean Eng. 118, 249–266.
Heinrich, P., Piatanesi, A., Hebert, H., 2001. Numerical modelling of tsunami generation and propagation from submarine slumps: the 1998 Papua New Guinea events. Geophys. J. Int. 145, 97–111.
Heller, V., Hager, W.H., Minor, H.-E., 2008. Scale effects in subaerial landslide generated impulse waves. Exp. Fluids 44 (5), 691–703.
Hoque A., 2002. Air bubble entrainment by breaking waves and associated energy dissipation. Ph.D. thesis, Dept of Architecture and Civil Eng., Toyohashi Univ. of Technology, Japan, 151 pp.
Hunt, B., 1988. Water waves generated by distant landslides. J. Hydraul. Res. 26, 307–322.
Imamura, F., Imteaz, M.M.A., 1995. Long waves in two-layers: governing equations and numerical model. Sci. Tsunami Hazards 14, 13–28.
Jiang, L., Leblond, P.H., 1992. The coupling of a submarine slide and the surface wave it generates. J. Geophys. Res. 97 (12), 731–744.
Jiang, L., Leblond, P.H., 1993. Numerical modeling of an underwater Bingham plastic mudslide and the wave which it generates. J. Geophys. Res. 98, 304–317.
Kataoka, I., 1986. Local instant formulation of two-phase flow. Int. J. Multiph. Flow 12 (5), 745–758.
LeVeque, R.J., 1990. Numerical methods for conservation laws. Lectures in Mathematics. Birkhauser, Zurich.
Li, J., 1995. Piecewise linear interface calculation. C. R. Acad. Sci, Paris, Série IIb 320, 391–396.
Liu P.L.F., 1999. Free surface tracking methods and their applications to wave hydrodynamics. Advances in Coastal and Ocean Engineering, Vol. 5. World Scientific, 213–240.
Liu, P.L.F., Lynett, P., Synolakis, C., 2003. Analytical solutions for forced long waves on a sloping beach. J. Fluid Mech. 478, 101–109.
Liu, P.L.F., Wu, T.R., Raichlen, F., Synolakis, C.E., Borrero, J.C., 2005. Run-up and run-down generated by three-dimensional sliding masses. J. Fluid Mech. 536, 107–144.
Løvholt, F., Harbitz, C.B., Haugen, K.B., 2005. A parametric study of tsunamis generated by submarine slides in the Ormen Lange/Storegga area off western Norway. Mar. Pet. Geol. 22, 219–231.
Løvholt, F., Pedersen, G., Gisler, G., 2008. Oceanic propagation of a potential tsunami from the La Palma Island. J. Geophys. Res. 113, C09026. doi:10.1029/2007JC004603.
Lubin, P., Vincent, S., Abadie, S., Caltagirone, J.P., 2006. Three-dimensional Large Eddy Simulation of air entrainment under plunging breaking waves. Coast. Eng. 53 (8), 631–655.
Lynett, P., Liu, P.L.F., 2005. A numerical study of the run-up generated by three-dimensional landslides. J. Geophys. Res. 110, C03006. doi:10.1029/2004JC002443.
Mader, C., Gittings, M.L., 2002. Modeling the 1958 Lituya Bay mega-tsunami, II. Sci. Tsunami Hazards 20 (5), 241–250.
Mader, C., Gittings, M.L., 2003. Dynamics of water cavity generation. Sci. Tsunami Hazards 21 (2), 91–101.
Masson, D., Watts, A.B., Gee, M.J.R., Urgeles, R., Michell, N.C., Le Bas, T.P., Canals, M., 2002. Slope failures on the flanks of the western Canary Islands. Earth Sci. Rev. 57, 1–35.
Masson, D.G., Harbitz, C.B., Wynn, R., Pedersen, G., Løvholt, F., 2006. Submarine landslides: processes, triggers and hazard prediction. Philos. Trans. R. Soc., A 364, 2009–2039.
Monaghan, J.J., Kos, A., 2000. Scott Russell's wave generator. Phys. Fluids 12 (3), 622–630.
Morichon, D., Abadie, S., 2010. Landslide generated impulse waves. Influence of initial slide shape and deformability (in French). La Houille Blanche. 1, no. spécial génie civil génie côtier. doi:10.1051/lhb/2010013.
Noda, E., 1970. Water waves generated by landslides. J. Waterw. Harb. Coast. Eng. Div. 96, 835–855.
Panizzo, A., Dalrymple, R.A., 2004. SPH modelling of underwater landslide generated waves. Proc. 29th Intl. Conference on Coastal Engineering, Lisbon. World Scientific Press, pp. 1147–1159.
Pararas-Carayannis, G., 2002. Evaluation of the threat of mega tsunamis generation from postulated massive slope failure of island stratovolvanoes on La Palma, Canary Islands, and on the island of Hawaii. Sci. Tsunami Hazards 20, 251.
Pareschi, M.T., Boschi, E., Favalli, M., 2006. Lost tsunami. Geophys. Res. Lett. 33, L22608. doi:10.1029/2006GL027790.
Pelinovsky, E., Poplavsky, A., 1996. Simplified model of tsunami generation by submarine landslides. Phys. Chem. Earth 21 (12), 12–17.
Peskin, C.S., 1977. Numerical analysis of blood flow in the heart. J. Comput. Phys. 25, 220–252.
Quecedo, M., Pastor, M., Herreros, M.I., 2004. Numerical modelling of impulse wave generated by fast landslides. Int. J. Numer. Methods Eng. 59, 1633–1656.
Randrianarivelo, T.N., Pianet, G., Vincent, S., Caltagirone, J.P., 2005. Numerical modeling of solid particle motion using a new penalty method. Int. J. Numer. Methods Fluids 47, 1245–1251.

Russel, J., 1844. Report on waves. Rep. Brit. Assoc. for the Advancement of Science, pp. 311–390.
Sagaut, P., 1996. Numerical simulations of separated flows with subgrid models. Rech. Aéro, pp. 1–63.
Tappin, D.R., Watts, P., Grilli, S.T., 2008. The Papua New Guinea tsunami of 1998: anatomy of a catastrophic event. Nat. Hazards Earth Syst. Sci. 8, 243–266 www.nat-hazards-earth-syst-sci.net/8/243/2008/.
Tinti, S., Pagnoni, G., Zaniboni, F., 2006. The landslides and tsunamis of the 30th of December 2002 in Stromboli analyzed through numerical simulations. Bull. Volcanol. 68, 462–470.
Van der Vorst, H.A., 1992. BI-CGSTAB: a fast and smoothly converging variant of BI-CG for the solution of nonsymmetric linear systems. SIAM J. Sei. Stat. Comput. 13, 631–644.
Varnes, D.J., 1978. Slope movements types and processes. In: Shuster, R.L., Krizek, R.J. (Eds.), Landslides Analysis and Control: Transportation Res. Board Spec. Rep., 176, pp. 11–33.
Vincent, S., Caltagirone, J.P., 1999. Efficient solving method for unsteady incompressible flow problem. Int. J. Numer. Methods Fluids 30, 795–811.
Vincent, S., Randrianarivelo, T.N., Pianet, G., Caltagirone, J.P., 2007a. Local penalty methods for flow interacting with moving solids at high Reynolds numbers. Comput. Fluids 36, 902–913.
Vincent, S., Larocque, J., Lubin, P., Caltagirone, J.P., Pianet, G., 2007b. Adaptative Augmented Lagrangian techniques fir simulating unsteady multiphase flows. 6th International Conference on Multiphase Flow, Leipzig, Germany.
Walder, J.S., Watts, P., Sorensen, O.E., Janssen, K., 2003. Tsunami generated by subaerial mass flows. J. Geophys. Res. 108 (B5), 2236. doi:10.1029/2001JB000707.
Ward, S.N., 2001. Landslide tsunami. J. Geophys. Res. 106 (6), 11201–11215.
Ward, S.N., Day, S., 2001. Cumbre Vieja Volcano — potential collapse and tsunami at La Palma, Canary Islands. Geophys. Res. Lett. 28, 397–400.
Watts P., 1997. Water waves generated by underwater landslides. PhD thesis, California Institute of Technology, Pasadena, Calif.
Watts, P., Grilli, S.T., Kirby, J.T., Fryer, G.J., Tappin, D.R., 2003. Landslide tsunami case studies using a Boussinesq model and a fully nonlinear tsunami generation model. Nat. Hazards Earth Syst. Sci. 3, 391–402.
Watts, P., Grilli, S.T., Tappin, D., Fryer, G.J., 2005. Tsunami generation by submarine mass failure Part II: predictive equations and case studies. J. Waterw. Port Coast. Ocean Eng. 131 (6), 298–310.
White F., 2002. Fluid Mechanics, Fifth edition, Mc Graw-Hill, ISBN: 0072831804.
Wu, T. R., 2004. A numerical study of three-dimensional breaking waves and turbulence effects. PhD Thesis, Cornell University.
Yim, S.C., Yuk, D., Panizzo, A., Di Risio, M., Liu, P.L.F., 2008. Numerical simulation of wave generation by a vertical plunger using RANS and SPH models. J. Waterw. Port Coast. Ocean Eng. 134 (3), 143–159.
Young, D.L., Morton, K.W., Baines, M.J., 1982. Time-dependent multi-material flow with large fluid distortion. Numerical Methods for Fluid Dynamics. Academic Press, New York.
Yuk, D., Yim, S.C., Liu, P.L.F., 2006. Numerical modeling of submarine mass-movement generated waves using RANS model. Comput. Geosci. 32 (7), 927–935.